Materials Today 93 (2026) 103203

Contents lists available at ScienceDirect

Materials Today

journal homepage: www.elsevier.com/locate/mattod

Demountable quinoidal semiconductor nanobackpacks modulate neuro-immune for amplifying second near-infrared photoimmunotherapy of breast cancer

Yijing Zhang [a,b,1], Guangkun Song [c,1], Gaoli Niu [a,d,1], Ruiyan Li [a,b], Xue Yuan [a,b], Nana Ran [a], Yulu Hu [a], Tianze Du [a], Yongsheng Chen [c], Yong Kang [a,b,*], Li Wang [a,b,*], Xiaoyuan Ji [a,b,e,*]

[a] Academy of Medical Engineering and Translational Medicine, Medical College, Tianjin University, Tianjin 300072, China
[b] State Key Laboratory of Advanced Medical Materials and Devices, Tianjin University, Tianjin 300072, China
[c] State Key Laboratory and Institute of Elemento-Organic Chemistry, Centre of Nanoscale Science and Technology and Key Laboratory of Functional Polymer Materials, Renewable Energy Conversion and Storage Center (RECAST), Tianjin Key Laboratory of Functional Polymer Materials, College of Chemistry, Nankai University, Tianjin 300071, China
[d] The First Affiliated Hospital of Henan Polytechnic University, Jiaozuo 454000, China
[e] Department of Gastric Surgery, Tianjin Medical University Cancer Institute & Hospital, National Clinical Research Center for Cancer; Tianjin Key Laboratory of Digestive Cancer; Tianjin's Clinical Research Center for Cancer, Tianjin 300060, China

ARTICLE INFO

Keywords:
Organic semiconductor nanoparticles
Cancer photoimmunotherapy
Second near-infrared
Neuro-immune
Responsive nanosystems

ABSTRACT

The inherent wide bandgap of organic materials and the complex resistance environment within tumors could lead to suboptimal efficacy in photoimmunotherapy. Demountable quinoidal semiconductor nanobackpacks enable second near-infrared (NIR-II) phototherapy while alleviating thermoresistance and the immunosuppressive microenvironment. The nanobackpack features a core of quinoidal acceptor–donor-acceptor (ADA) semiconductor molecule and calcium peroxide (CaO_2)-based nanovesicles, loaded with capsaicin nanoparticles through a pH-responsive linker. The quinoidal structures introduction-induced bandgap narrowing enhances the NIR-II photothermal and photodynamic efficacy of the organic material, while CaO_2 disrupts mitochondrial function to suppress adenosine triphosphate (ATP) production, thereby alleviating heat shock proteins (HSPs)-mediated thermoresistance and programmed cell death ligand 1 (PD-L1) stabilization. Moreover, capsaicin works synergistically with immunogenic cell death (ICD) to enhance dendritic cell (DC) maturation. Specifically, the acidic-triggered release of capsaicin nanoparticles activates transient receptor potential vanilloid subtype 1 (TRPV1) channels on sensory neurons. This activation further promotes DC maturation, leading to enhanced antigen presentation and T cell activation. Collectively, this multi-mechanistic approach of the nanobackpack triggers potent antitumor immunity, resulting in nearly complete tumor suppression. This work overcomes the inherent limitations of organic photosensitizers and multiple resistance mechanisms in immunotherapy, offering an effective NIR-II combinational photoimmunotherapy strategy for breast cancer.

Introduction

Breast cancer remains the most prevalent malignancy worldwide, posing a significant threat to global public health [1,2]. Breast cancer caused approximately 670,000 deaths worldwide, with an estimated 2.3 million new cases in 2022, and its earlier onset is increasing pressure on healthcare resources and further raising the societal burden of disease, which cannot be overlooked [3,4]. Among its various subtypes, triple-negative breast cancer (TNBC) represents a particularly aggressive clinical challenge [5–7]. Characterized by the absence of estrogen receptor, progesterone receptor, and HER2 expression, TNBC accounts for 15–20% of all breast cancer cases and is associated with a disproportionately high risk of early metastasis, therapeutic resistance, and poor prognosis [2,8]. The five-year survival rate for metastatic TNBC remains

* Corresponding authors at: Academy of Medical Engineering and Translational Medicine, Medical College, Tianjin University, Tianjin 300072, China.
E-mail addresses: kangyong@tju.edu.cn (Y. Kang), wangli9@tju.edu.cn (L. Wang), jixiaoyuan@tju.edu.cn (X. Ji).
[1] These authors contributed equally to this work.

https://doi.org/10.1016/j.mattod.2026.103203
Received 29 October 2025; Received in revised form 13 January 2026; Accepted 22 January 2026
Available online 31 January 2026

strikingly low compared to other subtypes, and patients have limited treatment options, relying primarily on chemotherapy which often leads to drug resistance and disease relapse [9–11]. This underscores a critical, unmet clinical need for novel and effective therapeutic strategies.

In contrast to comprehensive treatments based on radiotherapy and chemotherapy, which often cause significant adverse effects, phototherapy has emerged as a promising modality with high spatiotemporal specificity [12,13]. It relies on photosensitive agents to mediate tumor ablation via localized hyperthermia and/or reactive oxygen species (ROS) generation [14,15]. Unlike inorganic materials, which often suffer from poor biodegradability and potential long-term toxicity, organic materials exhibit distinct advantages in near-infrared phototherapy due to their well-defined chemical structures and superior biocompatibility [16–18]. However, the energy conversion efficiency and tissue penetration depth of conventional organic agents are often limited by their relatively large bandgaps [19]. N-type small-molecule organic semiconductor with an acceptor-donor-acceptor (ADA) framework, a promising organic photovoltaic material, exhibits a high power conversion efficiency attributable to its high crystallinity, minimal energy tail states, and optimal energy levels. Nonetheless, its optical absorption is confined to wavelengths below 1000 nm due to its intrinsic bandgap [20,21]. Notably, the incorporation of quinoidal structures could effectively narrow the bandgap, extending the absorption of organic materials into the second near-infrared (NIR-II) window [22]. This redshift enhances tissue penetration depth and improves the photothermal conversion efficiency [23,24]. Furthermore, the incorporation of quinoidal structures enhance photodynamic performance by promoting π-electron delocalization and thereby improving the efficiency of photoinduced electron transfer [25,26]. This molecular engineering strategy of quinoidal structures incorporation thus offers a promising avenue for advancing organic material-mediated phototherapy for tumors.

Despite extensive research efforts, the therapeutic efficacy of phototherapy remains constrained by factors beyond the intrinsic properties of photosensitive agents. Primarily, cellular heat defense mechanisms could directly impair the outcomes of photothermal therapy (PTT) efficacy by upregulation of heat shock proteins (such as, HSP70) [27,28]. Although combined strategies involving small-molecule HSPs inhibitors have been developed to enhance PTT efficacy, their action is often hampered by delayed intervention, failing to preemptively block HSPs synthesis [29,30]. Moreover, HSPs contribute to immune evasion by stabilizing programmed cell death ligand 1 (PD-L1) expression on tumor cells, thereby attenuating the response to immunotherapy [31]. Calcium-based materials could disrupt mitochondrial Ca^{2+} homeostasis, leading to mitochondrial damage and subsequent suppression of adenosine triphosphate (ATP), which is essential for HSPs chaperone function [32]. Thus, incorporating calcium-based components may alleviate heat defense and mitigate immune escape, thereby augmenting phototherapeutic performance. However, the immunosuppressive tumor microenvironment is shaped by multiple intertwined factors [33–35]. Inadequate infiltration and functional failure of immune cells within tumor tissues significantly compromise the effectiveness of immunotherapies, particularly due to impaired dendritic cell (DC) maturation and inadequate T cell activation [36,37]. Thus, developing multifunctional synergistic strategies capable of simultaneously eradicating primary tumors, overcoming local immunosuppression, and systemically activating antitumor immunity represents a critical and urgent challenge in the field of cancer immunotherapy.

Recent studies have revealed that the interplay within the neuroimmune-tumor axis plays a pivotal role in tumor progression and immune responses [38–43]. Sensory neurons, through the release of neuropeptides and other mediators, profoundly regulate the function of immune cells in the tumor microenvironment [44–49]. Capsaicin, a specific agonist of the transient receptor potential vanilloid subtype 1 (TRPV1) channel [50–52], can effectively activate sensory neurons to promote DC maturation and the secretion of interleukin-12 (IL-12) via neuropeptide release [53–55]. Mature DCs can efficiently present tumor antigens and secrete IL-12, driving naïve T-cell differentiation toward Th1 cells and enhancing the proliferation and activation of cytotoxic T lymphocytes, which provides a unique neural regulatory pathway for breaking immune tolerance and eliciting an immune response [56–58]. However, the systemic administration of capsaicin faces significant challenges, including severe side effects (e.g., intense pain and inflammatory reactions) and low targeted delivery efficiency [59–63]. Achieving controllable release of capsaicin at tumor sites while synergizing with other therapeutic modalities to maximize its neuroimmunomodulatory effects represents a cutting-edge direction in the development of combinatorial immunotherapy strategies.

In this study, a pH-responsive demountable nanobackpack was designed to regulate neuroimmune interactions for synergistic immunotherapy of breast cancer. Through electrostatic interactions, capsaicin nanoparticles can be attached to the surface of nanomicelles containing a photothermal converter (all-fused-ring quinoidal acceptor-donor-acceptor molecule, SCKN) and calcium peroxide (CaO_2) nanoparticles by modifying the surface with polyethyleneimine (PEI), resulting in the formation of this nanobackpack (SN_{CaC}) (Fig. 1a). In the acidic tumor microenvironment, capsaicin nanoparticles can dissociate from the nanobackpack system and activate sensory neurons by opening the TRPV1 channel, which can further promote IL-12 secretion and DC maturation. In addition, nanoparticles containing SKCN and CaO_2 exposed to a 1064 nm laser not only directly killed 4T1 tumor cells through combined phototherapy and Ca^{2+} overload [64–66] but also triggered immunogenic cell death (ICD) to promote DC maturation. Notably, phototherapy upregulates HSP70, which stabilizes PD-L1. This stabilization can be alleviated by Ca^{2+}-mediated mitochondrial dysfunction, which decreases adenosine triphosphate (ATP) levels [67–69]. Therefore, sensory neuron activation and ICD-promoted DC tumor antigen presentation combined with PD-L1 downregulation effectively relieved T cell inhibition, which effectively promoted T cell tumor infiltration and tumor regression (Fig. 1b). This strategy converts neural signals into immune signals and utilizes phototherapy and Ca^{2+} overload to disrupt PD-L1 adaptation, resulting in synergistic immune therapy through triple coordination among the nervous, immune, and metabolic systems.

Experimental section

Materials

Tetrahydrofuran (THF), chloroform ($CHCl_3$), ammonia, hydrogen peroxide (H_2O_2, 30% v/v), calcium chloride ($CaCl_2$), polyvinyl pyrrolidone (PVP, MW: 10000), ethanol, N-hydroxysuccinimide (NHS), 1-ethyl-3-(3-dimethylaminopropyl)carbodiimide (EDC), 1,3-diphenylisobenzofuran (DPBF), 9,10-anthracenediyl-bis(methylene)dimalonic acid (ABDA), and methyl-4-(1-hydroxy-2,2,6,6-tetramethylpiperidin-4-yl) phenyl (m-THPP) were purchased from Sigma-Aldrich. Capsaicin was purchased from MedChemExpress. A Cell Counting Kit-8 (CCK8) was purchased from Solarbio. The 2,7-dichlorodihy-drofluorescein diacetate (DCFH-DA), calcein/PI cell viability/cytotoxicity assay kit, DNA damage assay kit (γ-H2AX immunofluorescence), Fluo-4 AM (Ca^{2+} fluorescence probe), Annexin V-FITC/PI apoptosis detection kit, and mouse IL-12 ELISA kit were purchased from Beyotime Biotechnology. The HSP70 antibody for western blot was obtained from Affinity Biosciences. A JC-1 mitochondrial membrane potential assay kit was obtained from AbMole. Antibodies against calreticulin (CRT), high mobility group box 1 (HMGB1), heat shock protein 70 (HSP70), programmed death-ligand 1 (PD-L1) and c-fos for immunofluorescence were purchased from Abcam. 1,2-distearoyl-*sn*-glycero-3-phosphoethanolamine-methoxy polyethylene glycol (DSPE-mPEG), 1,2-distearoyl-*sn*-glycero-3-phosphoethanolamine-polyethylene glycol-carboxyl (DSPE-PEG-COOH) and polyethylenimine (PEI) were purchased from Xi'an Ruixi Biological Technology (Xi'an, China). DMEM, phenol red-free DMEM, 1640

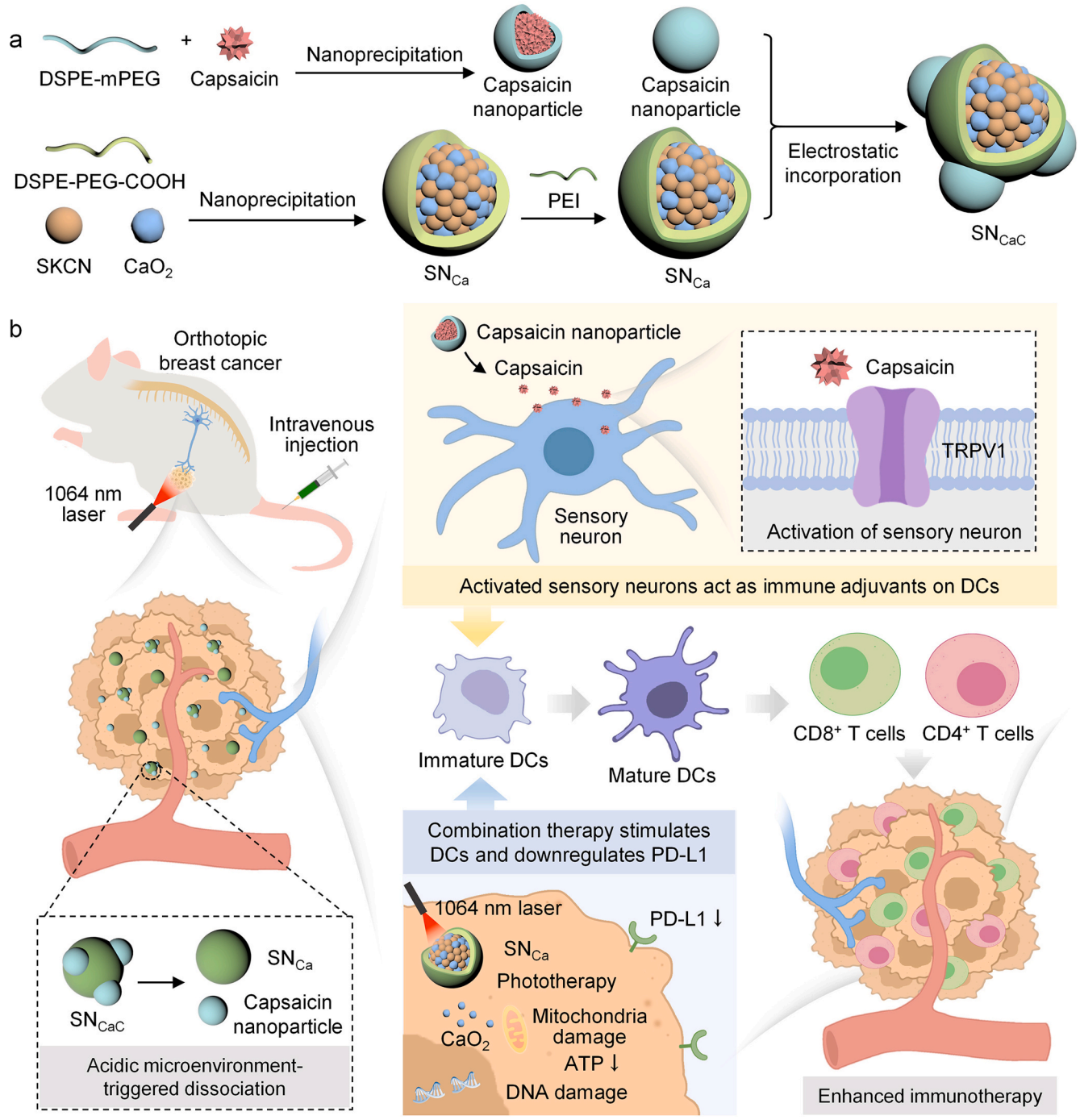

Fig. 1. Schematic diagram of SN_{CaC} for synergy photoimmunotherapy. (a) Schematic diagram of the preparation of the quinoidal semiconductor-based nano-backpack SN_{CaC}. (b) Mechanism of antitumor therapy via 1064 nm laser-mediated phototherapy and Ca^{2+} overload in combination with neuroenhanced immunotherapy.

medium, fetal bovine serum (FBS), trypsin-EDTA, and phosphate-buffered saline (PBS) were supplied by Gibco Life Technologies. Antibodies, including anti-CD45, anti-CD3, anti-CD4, anti-CD8, anti-CD25, anti-Foxp3, anti-CD11b, anti-CD11c, anti-CD80, and anti-CD86 antibodies, were obtained from Biolegend, Inc.

Methods

Synthesis and characterization of the compound SKCN

A solution of malononitrile (46 mg, 0.70 mmol) in THF (5 mL) was slowly added to sodium hydride (60% in oil, 40 mg, 1 mmol) at 0 °C, and the mixture was stirred for 1 h at room temperature (RT). To this suspension were added compound 1 (see Supplementary Fig. 1 for structure) (200 mg, 0.18 mmol) and tetrakis (triphenylphosphine)palladium (41.6 mg, 0.036 mmol). The mixture was heated at 70 °C for 8 h, and diluted hydrochloric acid (2 M, 10 mL) was added to an ice-cooling bath. The solution was extracted with dichloromethane, and 2,3-dicyano-5,6-dichlorobenzoquinone (DDQ, 81 mg, 0.36 mmol) was added. After stirring at room temperature for 1 h, the mixture was poured into water and then extracted with $CHCl_3$ (30 mL × 2), and the organic layer was dried over anhydrous $MgSO_4$. After removal of the solvent, the crude product was purified by silica gel and then recrystallized from $CHCl_3$

and methanol to obtain SKCN as a dark green solid (106 mg, 54%). The SKCN was characterized by ^{1}H NMR, ^{13}C NMR (a Bruker AV400 nuclear magnetic resonance spectrometer, $CDCl_3$), and high-resolution mass spectrometry. NMR spectra were processed using MestReNova, and HR-MS data were analyzed with Agilent MassHunter. Cyclic voltammetry (CV) was performed to determine the frontier orbital energy levels of SKCN and Y6. Measurements were conducted on thin films in acetonitrile with 0.1 mol L^{-1} *n*-Bu_4NPF_6 at a scan rate of 100 mV s^{-1}. The highest occupied molecular orbital (HOMO)/lowest unoccupied molecular orbital (LUMO) were calculated from the onset oxidation potential and the onset reduction potential versus FC/FC^+, using the equations $E_{HOMO} = -(4.80 + E^{ox}_{onset\ vs\ FC/FC+})$ and $E_{LUMO} = -(4.80 + E^{re}_{onset\ vs\ FC/FC+})$. The molar extinction coefficient is measured using Cary 5000 UV-vis-NIR spectrophotometer and further calculated. The mass change of the SKCN was recorded as a function of temperature (30 °C-800 °C) using a thermogravimetric analyzer.

Computational model and details

The structures were subjected to density functional theory (DFT) optimization in a vacuum environment via Gaussian 16 software. All the alkyl chains were replaced with methyl groups (–CH_3) to reduce the computational requirements. Following geometry optimization, vibrational frequencies were calculated, with no imaginary frequency found. Optimization, frequency analysis and energy level calculations were conducted via the B3LYP functional with a 6-31G(d) basis set. The calculations for the T1 excitation energy were conducted via time-dependent density functional theory (TD-DFT) at the B3LYP/6-31G(d) level.

Synthesis of CaO_2 nanoparticles

First, $CaCl_2$ (100 mg) and polyvinylpyrrolidone (PVP) (350 mg) were fully dissolved in 15 mL of ethanol. Then, 30% H_2O_2 (200 μL) solution and 1 mL of ammonia were slowly added to the above mixture under stirring conditions to obtain $CaCl_2$ nanoparticles. The product was collected via centrifugation (12000 rpm, 15 min), washed three times with ethanol, and subsequently dispersed in ethanol for storage at 4 °C.

Synthesis and characterization of SN_{CaC} nanoparticles

These nanoparticles were prepared via nanoprecipitation. First, nanoparticles loaded with capsaicin were prepared. Capsaicin (1 mg) and 1,2-Distearoyl-*sn*-glycero-3-phosphoethanolamine-methoxy polyethylene glycol (DSPE-mPEG) (40 mg) were fully dissolved in 1 mL of THF. The above solution was rapidly injected into a mixture of THF and water (1:9 vol ratio of THF to water) under sonication conditions for 30 min. Capsaicin-loaded nanoparticles were obtained after ultrafiltration and stored at 4 °C. Nanoparticles containing CaO_2 and SKCN (SN_{Ca}) were subsequently prepared via similar methods. Briefly, SKCN, CaO_2 and 1,2-distearoyl-*sn*-glycero-3-phosphoethanolamine-polyethylene glycol-carboxyl (DSPE-PEG-COOH) were mixed in THF at a mass ratio of 1:1:40, followed by rapid injection of a mixture system of THF and water and ultrasonication for 30 min. Pure SN_{Ca} was obtained by ultrafiltration. The ultrafiltration was performed using centrifugal filters (100 kDa MWCO) at 3000 rpm for 20 min per cycle at 4 °C, with deionized water as the wash solvent, repeated five times. To load capsaicin nanoparticles, SN_{Ca} was first dispersed with EDC (10 mg) and NHS (10 mg) in pure water and stirred for 2 h (at RT), followed by the addition of PEI and stirring for 3 h (at RT). Excess PEI was removed by ultrafiltration (same conditions). Capsaicin nanoparticles were subsequently stirred together with PEI-modified SN_{Ca} for 12 h (at RT), and pure capsaicin nanoparticle-coupled SN_{Ca} (SN_{CaC}) was obtained via ultrafiltration (same conditions). The morphology of these nanoparticles was observed via transmission electron microscopy (TEM, Tecnai G2F20, Holland). The hydrated particle size and surface potential of these nanoparticles were determined via a Litesizer 500 laser particle analyzer (Anton Paar, Austria). The spectra of the nanoparticles were determined via a Cary 5000 UV-vis-NIR spectrophotometer (Agilent, USA). The fluorescence spectra were measured via an FLS1000 steady-state and transient fluorescence spectrometer equipped with a xenon lamp excitation source (Edinburgh Instruments, UK).

Evaluation of pH-triggered capsaicin nanoparticle release

The morphology of SN_{CaC} stored for 4 h in a pH 6.5 solution was observed and imaged using TEM. SN_{CaC} was incubated in a solution with a pH of 6.5 for varying durations (1, 12, 24, and 48 h) and filtered through a polycarbonate membrane with a pore size of 0.05 μm to obtain dissociated capsaicin nanoparticles. The released capsaicin was detected via high-performance liquid chromatography. 2 mobile phase: methanol and water (7:3), 20 μL injection volume, 280 nm detection wavelength.

Stability assessment

SN_{CaC} was dispersed separately in PBS or serum and stored for 14 days. The particle size and zeta potential of SN_{CaC} were measured using a Litesizer 500 laser particle analyzer on day 0, day 7, and day 14.

Evaluation of the photothermal and photodynamic performance

The temperature change and thermal imaging of SN_{CaC} under 1064 nm laser irradiation were recorded via a thermal imaging camera. Different concentrations (0, 3, 6, 12, 25, 50, and 100 μg/mL) of SN_{CaC} solutions were irradiated with a 1064 nm laser at a power of 1.0 W/cm^2 for 5 min, the temperature changes were recorded at intervals of 30 s, and thermal images were collected. In addition, the SN_{CaC} solution (25 μg/mL) was exposed to continuous irradiation with a 1064 nm laser of different powers (0, 0.5, 1.0, and 1.5 W/cm^2), the temperature of the solution was recorded at 30 s intervals, and thermal images were collected. Furthermore, the SN_{CaC} solution (25 μg/mL) was exposed to 5 min of 1064 nm laser irradiation (1.0 W/cm^2) and cooled, and then, this system was irradiated again under the same conditions 5 times to evaluate the photothermal stability of SN_{CaC}. DPBF and ABDA were used to evaluate the performance of these nanoparticles for ROS generation under 1064 nm laser irradiation. DPBF (at a final concentration of 60 μg/mL) was mixed with different concentrations (0, 6, 12, 25, 50, and 100 μg/mL) of SN_{CaC} and irradiated with a 1064 nm laser (1.0 W/cm^2) for 10 min. During this period, the UV-visible spectra of the above solutions were measured at 1 min intervals, and the absorbance at 420 nm was recorded. In a manner similar to the operation described above, the absorbance of DPBF under 1064 nm laser irradiation at different powers (0, 0.5, 1.0, and 1.5 W/cm^2) was measured, and spectra were collected. In addition, different concentrations (0, 6, 12, 25, 50, and 100 μg/mL) of SN_{CaC} solutions containing ABDA (final concentration of 62.5 μg/mL) were irradiated with a 1064 nm laser (1.0 W/cm^2) for 10 min, and the absorbance at 400 nm and the UV-visible spectra of ABDA were detected and collected every 2 min of irradiation. Similarly, UV-visible spectra of the ABDA solution mixed with SN_{CaC} after 1064 nm laser irradiation at different powers (0, 0.5, 1.0, and 1.5 W/cm^2) were detected and collected.

Similar to the above evaluation methods, the photothermal and photodynamic performance of BTP-4F (Y6) under 1064 nm laser irradiation was assessed. Y6 nanoparticles were first prepared via nanoprecipitation. To evaluate the photothermal properties, temperature increases were recorded using a thermal imaging camera for Y6 solutions of different concentrations (0, 6, 12, 25, 50, and 100 μg/mL) under 1064 nm laser irradiation at 1.5 W/cm^2, as well as for a 100 μg/mL Y6 solution under varying laser powers (0, 0.5, 1.0, and 1.5 W/cm^2). In addition, ROS generation by Y6 was evaluated using DPBF and ABDA probes. For DPBF assays, solutions containing different Y6 concentrations (0, 6, 12, 25, 50, and 100 μg/mL) and DPBF (final concentration: 60 μg/mL) were irradiated with a 1064 nm laser (1.5 W/cm^2) for 10 min. UV-visible spectra were collected every minute, and absorbance at 420 nm was recorded. Similarly, solutions containing Y6 (100 μg/mL) and DPBF (at a final concentration of 60 μg/mL) were irradiated with different laser powers (0, 0.5, 1.0, and 1.5 W/cm^2) under the same protocol. For ABDA assays, solutions with varying Y6 concentrations (0,

6, 12, 25, 50, and 100 μg/mL) and ABDA (final concentration of 62.5 μg/mL) were irradiated at 1.5 W/cm^2 for 10 min, and absorbance at 400 nm was recorded each minute. Correspondingly, solutions containing Y6 (100 μg/mL) and ABDA (final concentration of 62.5 μg/mL) were exposed to different laser powers (0, 0.5, 1.0, and 1.5 W/cm^2) following the same spectral acquisition procedure.

Evaluation of cell uptake

Different nanoparticles were labeled with methyl-4-(1-hydroxy-2,2,6,6-tetramethylpiperidin-4-yl)phenyl (m-THPP) to evaluate their uptake behavior by 4T1 cells. 4T1 cells were seeded in 20 mm glass bottom cell culture dishes and treated with PBS, SN, CaO_2, SN_{Ca}, and SN_{CaC} (at a concentration of 25 μg/mL based on SKCN or CaO_2) for 6 h. Then, the cells were washed and fixed, and nuclei were stained with 4′,6-diamidino-2-phenylindole dihydrochloride (DAPI). The uptake of these materials by 4T1 cells was observed and imaged using laser scanning confocal microscopy (LSCM), followed by quantitative analysis with ImageJ software.

Evaluation of intracellular calcium

To load the Ca^{2+} assay fluorescence probe (Fluo-4 AM), 4T1 cells were first incubated with Fluo-4 AM for 1 h in the dark. Then, the 4T1 cells were incubated with different nanoparticles (at a concentration of 25 μg/mL based on SKCN or CaO_2). The intracellular calcium images and green fluorescence intensity were collected and quantified via fluorescence microscopy and ImageJ, respectively.

Evaluation of the cytotoxicity and therapeutic effect

To evaluate the cytotoxicity of these nanoparticles, 4T1 cells (1×10^4) were first seeded in 96-well plates and then treated with SN, CaO_2, SN_{Ca}, or SN_{CaC} at different concentrations (0, 3, 6, 12, 25, 50, or 100 μg/mL) for 24 h. The cytotoxicity of these nanoparticles was then analyzed via the CCK-8 assay. In addition, the viability of 4T1 cells incubated with PBS, SN, CaO_2, and SN_{Ca} (at a concentration of 25 μg/mL based on SKCN or CaO_2) without/with 1064 nm laser irradiation (1.0 W/cm^2, 5 min) was measured via a CCK-8 assay to investigate the treatment effects of these nanoparticles. During laser irradiation, replace the DMEM with phenol red-free DMEM and open the lid of the cell culture plate.

Live/death staining and apoptosis assessment

4T1 cells seeded in 24-well plates were co-incubated with PBS, SN, CaO_2 and SN_{Ca} (at a concentration of 25 μg/mL based on SKCN or CaO_2) for 12 h prior to light irradiation. After the light treatment (1064 nm laser, 1.0 W/cm^2, 5 min), staining was performed using a calcein/PI cell viability/cytotoxicity assay kit. Replace the DMEM with phenol red-free DMEM before laser irradiation and keep the lid open during the irradiation process. Observation and imaging were carried out with a fluorescence microscope. In addition, 4T1 cells incubated with PBS, SN, CaO_2 and SN_{Ca} (at a concentration of 25 μg/mL based on SKCN or CaO_2) and subjected to laser treatment (1064 nm laser, 1.0 W/cm^2, 5 min) were collected and prepared as single-cell suspensions. Staining was conducted using an Annexin V-FITC/PI apoptosis detection kit, followed by detection via flow cytometry and data processing with FlowJo software.

Evaluation of intracellular ROS generation

4T1 cells were seeded in a 24-well plate (5×10^4 cells/well) and then incubated with PBS, SN, CaO_2, and SN_{Ca} (at a concentration of 25 μg/mL based on SKCN or CaO_2) for 12 h. Subsequently, DCFH-DA (0.2 μM) was added, and the 4T1 cells were exposed to a 1064 nm laser (1.0 W/cm^2, 5 min). Replace the DMEM with phenol red-free DMEM before laser irradiation and keep the lid open during the irradiation process. The production of ROS was observed via fluorescence microscopy, and the fluorescence intensity was quantified via ImageJ.

Evaluation of the mitochondrial membrane potential

To evaluate the change in the mitochondrial membrane potential, 4T1 cells treated with PBS, SN, CaO_2, and SN_{Ca} (at a concentration of 25 μg/mL based on SKCN or CaO_2) without/with 1064 nm laser irradiation (1.0 W/cm^2, 5 min) were washed and stained with JC-1 (1 μg/mL) for 20 min. LSCM was used to obtain fluorescence images of JC-1, and ImageJ was used to quantify the fluorescence intensity. Moreover, 4T1 cells were seeded in 20 mm glass bottom cell culture dishes and incubated with 10 μM BAPTA-AM. After treatment with PBS, CaO_2, or SN_{Ca} nanoparticles (at a concentration of 25 μg/mL based on SKCN or CaO_2), the BAPTA-AM loaded 4T1 cells were irradiated by 1064 nm laser irradiation (1.0 W/cm^2) for 5 min. Subsequently, staining was performed using JC-1 dye, and images were captured and observed by a LSCM. The fluorescence intensity was quantified via ImageJ. Replace the DMEM with phenol red-free DMEM before laser irradiation and keep the lid open during the irradiation process.

Evaluation of the DNA damage

4T1 cells treated with PBS, SN, CaO_2, and SN_{Ca} (at a concentration of 25 μg/mL based on SKCN or CaO_2) without/with 1064 nm laser irradiation (1.0 W/cm^2) were fixed and immunofluorescence staining for γ-H2AX was performed to assess DNA damage. Replace the DMEM with phenol red-free DMEM before laser irradiation and keep the lid open during the irradiation process. LSCM was used to obtain fluorescence images of γ-H2AX, and ImageJ was used to quantify the fluorescence intensity.

Evaluation of intracellular ATP levels

4T1 cells were seeded in 24-well plates and treated with PBS, SN, CaO_2, or SN_{Ca} nanoparticles (at a concentration of 25 μg/mL based on SKCN or CaO_2) 12 h prior to irradiation with a 1064 nm laser (1.0 W/cm^2, 5 min). After different treatments, 4T1 cells in each group were collected and lysed for ATP level evaluation using an ATP assay kit. In addition, 4T1 cells were incubated with 10 μM BAPTA-AM and treated with PBS, CaO_2, or SN_{Ca} nanoparticles (at a concentration of 25 μg/mL based on SKCN or CaO_2). After co-incubation for 12 h and irradiation with/without a 1064 nm laser (1.0 W/cm^2, 5 min), 4T1 cells were collected and lysed for ATP level evaluation using an ATP assay kit. Replace the DMEM with phenol red-free DMEM before laser irradiation and keep the lid open during the irradiation process.

Evaluation of the HSP70 expression

The expression level of HSP70 in 4T1 cells following different treatments was assessed using immunofluorescence staining and western blot. 4T1 cells were seeded in 20 mm glass bottom cell culture dishes and treated with PBS, SN, CaO_2, or SN_{Ca} (at a concentration of 25 μg/mL based on SKCN or CaO_2) for 12 h, with/without 1064 nm laser irradiation (1.0 W/cm^2, 5 min). The cells were then fixed with 4% paraformaldehyde solution for subsequent immunofluorescence staining of HSP70. Fluorescence images were acquired and observed using a LSCM. In addition, after different treatments, 4T1 cells were lysed for protein extraction, and HSP70 expression was evaluated via western blot. Moreover, 4T1 cells loaded with BAPTA-AM were treated with PBS, CaO_2, and SN_{Ca} (at a concentration of 25 μg/mL based on SKCN or CaO_2), respectively, followed by 1064 nm laser irradiation (1.0 W/cm^2, 5 min) or no irradiation, and then fixed for HSP70 immunofluorescence staining. Nuclei were counterstained with DAPI. Observation and imaging were performed using a LSCM, and the fluorescence intensity was quantified via ImageJ. Replace the DMEM with phenol red-free DMEM before laser irradiation and keep the lid open during the irradiation process.

Evaluation of PD-L1 levels

4T1 cells (1×10^5) were seeded in 20 mm glass bottom cell culture dishes. After coincubation with PBS, SN, CaO_2, and SN_{Ca} nanoparticles (at a concentration of 25 μg/mL based on SKCN or CaO_2) for 12 h and

irradiation with a 1064 nm laser (1.0 W/cm^2, 5 min), 4T1 cells were fixed with 4% paraformaldehyde to perform immunofluorescence staining for PD-L1. The cell nuclei were stained with DAPI. The fluorescence images were obtained via LSCM, and the fluorescence intensity was quantified via ImageJ. 4T1 cells were seeded in 20 mm glass bottom cell culture dishes and loaded with BAPTA-AM. Then, 4T1 cells treated with PBS, CaO_2, and SN_{Ca} (at a concentration of 25 μg/mL based on SKCN or CaO_2) respectively, followed by 1064 nm laser irradiation (1.0 W/cm^2, 5 min) or no irradiation. 4T1 cells from each group were washed and fixed for PD-L1 immunofluorescence staining. Cell nuclei were labeled with DAPI. Fluorescence images were captured by LSCM and quantitatively analyzed using ImageJ. Replace the DMEM with phenol red-free DMEM before laser irradiation and keep the lid open during the irradiation process.

Evaluation of in vitro immunogenic cell death (ICD) and dendritic cell (DC) maturation

The ICD effect induced by these nanoparticles was evaluated by measuring the levels of high mobility group box 1 (HMGB1) and calreticulin (CRT) as well as the DC maturation. 4T1 cells (1×10^5) were seeded in 20 mm glass bottom cell culture dishes and exposed to PBS, SN, CaO_2, and SN_{Ca} nanoparticles (at a concentration of 25 μg/mL based on SKCN or CaO_2) without/with 1064 nm laser irradiation (1.0 W/cm^2, 5 min). Replace the DMEM with phenol red-free DMEM before laser irradiation and keep the lid open during the irradiation process. After that, the 4T1 cells were fixed, and immunofluorescence staining was performed for HMGB1 and CRT, followed by LSCM observation of the levels of HMGB1 and CRT. The fluorescence intensity was measured by ImageJ. To assess the maturation of DCs induced by ICD, bone marrow-derived DCs isolated from the femurs and tibiae of 6-week-old BALB/c mice were seeded in 6-well plates and cultured in media containing colony-stimulating factor (CSF) and interleukin-4 (IL-4). After 6 days of cultivation, bone marrow-derived DCs (BMDCs) and 4T1 cells were transferred to the basal chamber and apical chamber of the transwell system, respectively, followed by treatment with PBS, SN, CaO_2, and SN_{Ca} nanoparticles (at a concentration of 25 μg/mL based on SKCN or CaO_2) without/with laser irradiation (1064 nm laser, 1.0 W/cm^2, 5 min). Replace the DMEM with phenol red-free DMEM before laser irradiation and keep the lid open during the irradiation process. After 24 h, the BMDCs from the basal chamber were collected and stained with anti-CD11c, anti-CD86, and anti-CD80 antibodies for flow cytometry analysis. The data were processed by FlowJo.

Establishment of an orthotopic breast cancer mouse model and evaluation of in vivo therapeutic effect

Six- to eight-week-old BALB/c female mice from Beijing SiPeiFu Laboratory Animal Co., Ltd. (China) were utilized in this study. These BALB/c mice were maintained in a specific pathogen-free environment with the temperature regulated at 23–26 °C and the humidity maintained between 40–60% under a 12 h light/12 h dark cycle. Each cage housed 3–5 mice, which were allowed free access to food and water. All animal procedures adhered to the guidelines for the use and care of laboratory animals at Tianjin University and were approved by the Tianjin University Institutional Animal Care and Use Committee (IACUC), with the approval number TJUE2025-A-S-013.

Orthotopic breast cancer models were established by in situ inoculation of 4T1 cells. Briefly, the fourth mammary fat pad of each anesthetized and depilated mouse was injected with 50 μL of 4T1 cell suspension (2×10^6 cells per mouse). Treatment was initiated when the tumor volume reached 70–100 mm^3. Mice were randomly divided into 6 groups (n = 5 per group) and treated with PBS, SN_{Ca}, SN_{CaC}, SN + laser, SN_{Ca} + laser, or SN_{CaC} + laser. Intravenous administration was measured at 200 μL per mouse (SKCN concentration = 150 μg/mL), and the 1064 nm laser was irradiated at a power of 1.0 W/cm^2 for 10 min per mouse. After administration, body weight and tumor volume were measured every other day. At the end of the treatment (at day 14), the mice were euthanized to isolate the tumors and major organs, the tumors were weighed, and sections of the tumors were prepared for hematoxylin and eosin (H&E) staining and terminal deoxynucleotidyl transferase dUTP nick end labeling (TUNEL) staining. Moreover, tumors from the mice in the PBS and SN_{CaC} + laser groups were collected at the end of treatment for RNA sequencing analysis by Novogene Co., Ltd.

Biodistribution and tumor accumulation

The fluorescent molecule m-THPP was doped into SN, SN_{Ca}, and SN_{CaC} to facilitate monitoring of the biodistribution of these nanoparticles after administration. The constructed orthotopic breast cancer model mice were randomly grouped (n = 3 per group) and injected with 200 μL of SN, SN_{Ca} or SN_{CaC} (SKCN concentration = 150 μg/mL) through the tail vein. The tumor fluorescence intensity at different time points was monitored via an in vivo imaging system. The mice were euthanized to isolate the heart, liver, spleen, lungs, kidneys and tumors, and the distribution of these nanoparticles in major organs and tumor sites was evaluated via an in vivo imaging system. Living Image® was used to quantify the fluorescence intensity.

Impact of sensory nerve signals on 4T1 tumor cells and DCs

Dorsal root ganglia (DRG) cells were coincubated with capsaicin nanoparticles (20 μg/mL) for 1 h, and the c-fos of the DRG cells was stained by immunofluorescence. DRG cells were seeded in the upper chamber of the Transwell system and stimulated with capsaicin. 4T1 cells or bone marrow-derived DCs (BMDCs) were seeded in the lower chamber of the Transwell system. The viability of 4T1 cells was determined via the CCK-8 method. For BMDCs, the lower chamber culture medium was collected, and interleukin-12 (IL-12) secretion was evaluated via enzyme-linked immunosorbent assay. Additionally, a similar Transwell system was used to further evaluate DC maturation. DRG cells and BMDCs were seeded in the upper and lower chambers, respectively. Capsaicin nanoparticles (20 μg/mL) were either added or not added to the upper chamber medium. Supernatant from 4T1 cells treated with SN_{Ca} (25 μg/mL) and 1064 nm laser irradiation (1 W/cm^2, 5 min) (later referred to as "supernatant" in the manuscript and Fig. 7d), serving as a source of damage-associated molecular patterns (molecules released by tumor cells during ICD), was either added or omitted from the lower chamber medium. Replace the DMEM with phenol red-free DMEM before laser irradiation and keep the lid open during the irradiation process. After different treatments, BMDCs were collected, prepared as single-cell suspensions, and subjected to flow cytometry staining and analysis. Data were processed using FlowJo.

Evaluation of the in vivo immune response

To explore the immune responses triggered by this treatment strategy, orthotopic breast cancer-bearing mice were first constructed. On the 5 day after administration, the tumor-draining lymph nodes (TDLNs), tumor tissue and spleens of the mice were isolated and processed into cell suspensions for subsequent staining. The cells from TDLNs were stained with anti-CD11c, anti-CD80 and anti-CD86 antibodies to evaluate DC maturation via flow cytometry. The tumors were stained with anti-CD45, anti-CD3, anti-CD4, anti-CD8a, anti-CD11c, anti-CD80, anti-CD86, anti-CD25, and anti-Foxp3 antibodies, and the levels of DCs, $CD4^+$ T cells, $CD8^+$ T cells, and regulatory T (T_{reg}) cells were analyzed via flow cytometry. Finally, cells from the spleen were labeled with anti-CD3, anti-CD4, and anti-CD8a antibodies to analyze $CD4^+$ T cells and $CD8^+$ T cells via flow cytometry. The data were processed via FlowJo.

In vivo biosafety assessment

Sections of major organs (heart, liver, spleen, lung and kidney) from the mice in each treatment group were prepared for H&E staining to evaluate histopathological changes. In addition, the body weights of the mice were monitored every other day during treatment. Moreover, healthy BALB/c mice were intravenously injected with PBS or SN_{CaC}

nanobackpacks (150 μg/mL, 200 μL per mouse). On days 1, 7, and 14, serum biochemical indicators including aminotransferase (ALT), alanine aspartate aminotransferase (AST), alkaline phosphatase (ALP), creatinine (CRE), and blood urea nitrogen (BUN) were evaluated to estimate the biocompatibility of SN_{CaC} nanobackpacks.

Elimination behavior of the SN_{CaC}

To evaluate the elimination behavior of the SN_{CaC}, mice (6–8-week-old female BALB/c, n = 3) were intravenously administered with m-THPP-labeled SN_{CaC} (SKCN concentration = 150 μg/mL, 200 μL per mouse). Feces samples were collected before administration and at 1, 2, 3, 5, 7, 14, and 21 days post-administration. Fluorescence images of the mice and feces were captured using an in vivo imaging system on the indicated days, and fluorescence intensity was recorded. On day 21 post-administration, the mice were euthanized, and the heart, liver, spleen, lungs, and kidneys were excised. Fluorescence images of the isolated organs were also acquired with the imaging system, and fluorescence intensity was measured.

Statistics and reproducibility

All data were described as mean ± standard deviation (SD) and the sample numbers (n) are provided. The significant differences (*$p < 0.05$, ** $p < 0.01$ and *** $p < 0.001$) between the experimental data were analyzed via one-way ANOVA and t tests.

Results and discussion

Construction and characterization of SKCN and nanobackpack

First, SKCN and CaO_2 nanoparticles were prepared. 2, 10-dibromo-12, 13-bis (2-ethylhexyl)-3,9-diundecyl-12, 13-dihydro-[1,2,5] thiadiazolo [3–9] thieno [2′‘,3′”:4′,5′] thieno [2′,3′:4,5] pyrrolo [3,2-g] thieno

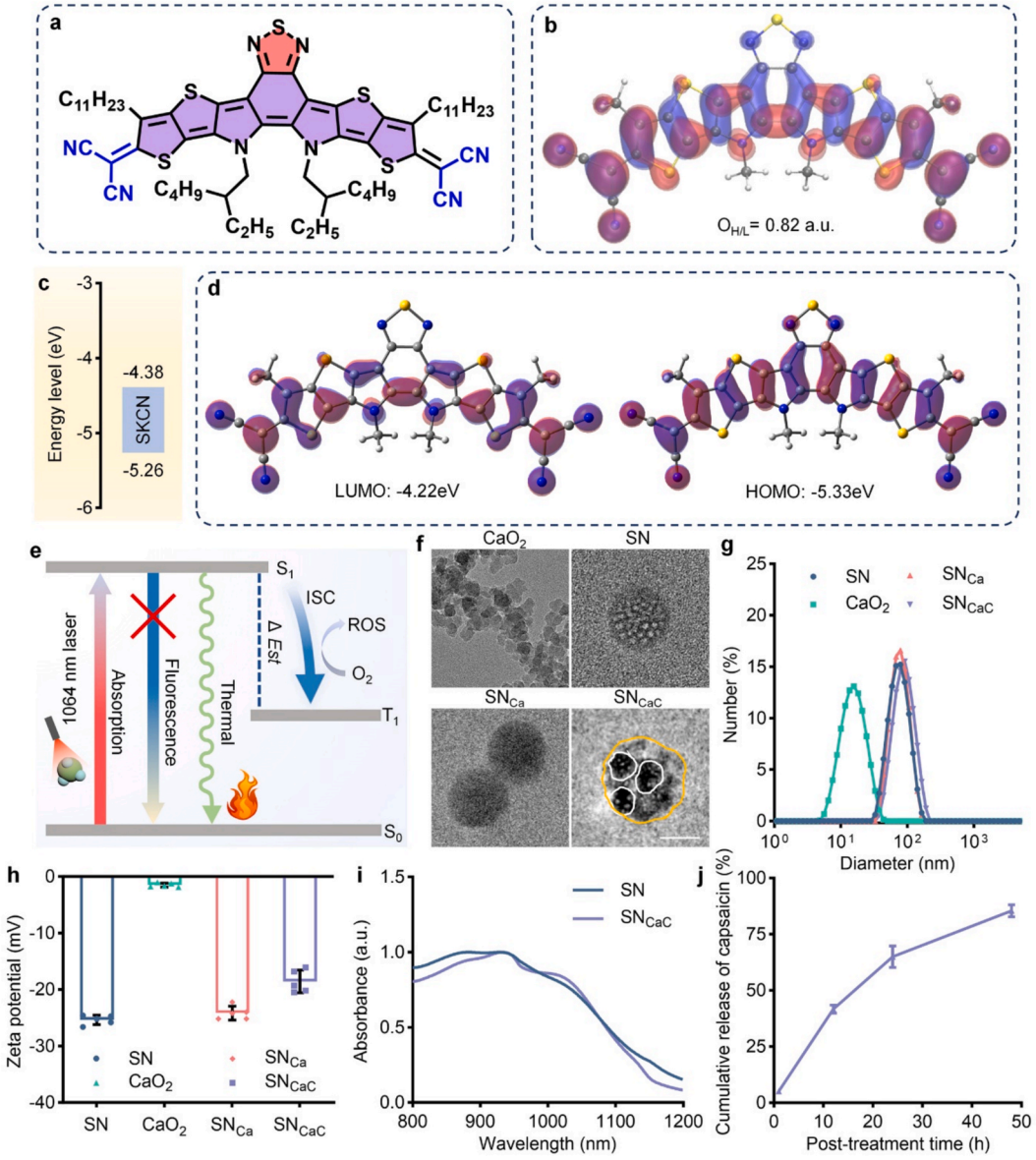

Fig. 2. Characterization of SKCN and different nanoparticles. (a) Molecular structure of the photothermal conversion compound SKCN. (b) Molecular orbitals and energy diagrams at the B3LYP/6-31G(d) level. $O_{H/L}$ represents the overlap integral between the HOMO and LUMO. (HOMO: orange, LUMO: blue). (c) Energy level diagram of SKCN. (d) Molecular structures and theoretical density distributions of the frontier molecular orbits of the HOMO and LUMO for SKCN, which were calculated via the DFT method. (e) Simulated Jablonski diagram of energy conversion between different energy levels of the SKCN molecule. (f) Representative TEM images of CaO_2, SN, SN_{Ca} and SN_{CaC} (scale bar = 50 nm). Diameters (g) and zeta potentials (h) of CaO_2, SN, SN_{Ca} and SN_{CaC} (n = 5). (i) UV-Vis-NIR spectra of SN and SN_{CaC}. (j) Cumulative release of capsaicin from SN_{CaC} (pH = 6.5) (n = 3).

[2′,3′:4,5] thieno [3,2-b] indole coupled with malononitrile and oxidized by DDQ could lead to SKCN, which features a quinoidal BTP core (Fig. 2a and Supplementary Fig. 1) [70]. All spectral data matched the expected structure (Supplementary Fig. 2-4). $O_{H/L}$ represents the overlap integral between the highest occupied molecular orbital (HOMO) and lowest unoccupied molecular orbital (LUMO). The $O_{H/L}$ value of SKCN was calculated to be 0.82 a.u. (Fig. 2b). A high $O_{H/L}$ value for SKCN indicated greater electron localization performance, which represented a stronger light absorption capacity for SKCN. The HOMO and LUMO of SKCN, as determined by cyclic voltammetry, were −5.26 eV and −4.38 eV (Fig. 2c). The HOMO and LUMO of SKCN estimated via DFT calculations were −5.33 eV and −4.22 eV, respectively, and the bandgap was calculated to be 1.10 eV (Fig. 2d). The lower energy level allowed SKCN to have a high light energy absorption efficiency, and the absorbed light could be converted into heat through nonradiative pathways (Fig. 2e). The molar extinction coefficient (ε) of SKCN was determined to be 0.81 × 10^5 m^{-1} cm^{-1}, demonstrating its pronounced light-absorbing capability, as shown in Supplementary Fig. 5. Furthermore, as shown by fluorescence spectra, no fluorescence emission was observed from SKCN in either its dissolved state or as nanoparticles (Supplementary Fig. 6). This observation aligns with the bandgap law depicted in Jabronski's diagram, wherein a reduced bandgap promotes non-radiative decay pathways over radiative ones, thereby effectively suppressing fluorescence and enhancing thermal conversion. To construct the SKCN-based nanobackpack system, CaO_2 nanoparticles were first synthesized in an ethanol solution using $CaCl_2$, ammonia, and H_2O_2 as substrates [71]. Then, nanoparticles containing SKCN and CaO_2 (defined as SN_{Ca}) as well as capsaicin nanoparticles were prepared via nanoprecipitation. Further modification of polyethyleneimine (PEI) on the surface of SN_{Ca} through amide reactions to adsorb capsaicin nanoparticles yielded this nanobackpack system (defined as SN_{CaC}). Nanoparticles loaded with SKCN (SN), CaO_2, and those containing SKCN and CaO_2 (SN_{Ca}) were used for comparison.

Characterization of these nanoparticles was first performed. Transmission electron microscopy (TEM) images revealed that the CaO_2 nanoparticles had a relatively homogeneous morphology of 16.7 ± 1.5 nm. SN and SN_{Ca} had similar spherical morphologies. The attachment of nearly spherical nanoparticles was observed on the surface of SN_{CaC}, which corroborated the successful synthesis of SN_{CaC} (Fig. 2f). The results of dynamic light scattering revealed that the sizes of CaO_2 (16.5 nm), SN (75.8 nm), SN_{Ca} (77.4 nm) and SN_{CaC} (90.4 nm) were similar to those observed via TEM (Fig. 2g). The zeta potential of CaO_2 was −1.5 mV. SN (−25.4 mV) and SN_{Ca} (−24.2 mV) had similar but lower surface potentials than did SN_{CaC} (−18.58 mV), which could be attributed to the different surface modifications (Fig. 2h). The stability and potential biosafety of SN_{CaC} in physiological environments were assessed by evaluating changes in particle size and zeta potential over different storage times in PBS buffer or serum. Over time, there were no significant changes in the particle size or zeta potential of SN_{CaC} in either PBS buffer or serum, indicating good colloidal stability and low aggregation tendency (Supplementary Fig. 7). SN and SN_{CaC} exhibited similar UV-Vis-NIR spectra with a maximum absorption peak at approximately 940 nm, which indicated that the light absorption of SKCN was not significantly affected (Fig. 2i). The behavior of SN_{CaC} nanobackpacks under acidic conditions was examined via TEM. Clear separation was observed between the capsaicin nanoparticles (highlighted by white circles) and the core micelle composed of SKCN and CaO_2 (indicated by orange-yellow circles) (Supplementary Fig. 8). In addition, capsaicin release from SN_{CaC} was evaluated via high-performance liquid chromatography (HPLC). Compared with SN_{CaC} treated in neutral solution (pH = 7.4), capsaicin release was detected from SN_{CaC} incubated in acidic solution (pH = 6.5) (Supplementary Fig. 9). The release of capsaicin increased over time, reaching 85.4% after 48 h of co-incubation (Fig. 2j).

Evaluation of photothermal conversion and photodynamic performance

To evaluate the photothermal and photodynamic performance of the SN_{CaC} system, we first investigated its photothermal conversion efficiency under 1064 nm NIR-II laser irradiation. The design of SKCN employs a ladder-type multifused ring structure, with a core consisting of multiple thiophene units and benzothiadiazole (BT). The fusion of multiple thiophene rings endows the central core with sufficient electron-donating ability. By fusing the central core with the strong electron-withdrawing unit malononitrile, SKCN exhibits distinct acceptor–donor-acceptor (ADA) characteristics (Fig. 3a). As a quinoidal small-molecule semiconductor featuring an ADA architecture, SKCN has a highly delocalized π-conjugated backbone with strong intramolecular charge transfer (ICT) characteristics. This unique molecular configuration enables SKCN to display a narrow bandgap (1.10 eV), facilitating efficient absorption in the NIR-II window and promoting rapid nonradiative decay pathways, which are essential for robust photothermal conversion. Upon 1064 nm irradiation at a power of 1.0 W/cm^2, the SN_{CaC} solutions presented a concentration-dependent temperature increase, with the temperature increasing by 30.6 °C at an SKCN concentration of 100 μg/mL after 5 min of irradiation (Fig. 3b and c). Even under low-power irradiation (0.5 W/cm^2), SN_{CaC} at 25 μg/mL induced a notable temperature increase of 14.2 °C (Fig. 3d and e). The photothermal stability of the system was confirmed by multiple heating–cooling cycles, which maintained consistent thermal output over five on/off irradiation sequences (Fig. 3f), indicating excellent photothermal durability, a hallmark of stable ADA-based semiconductors. Thermogravimetric analysis indicated that the primary decomposition of SKCN occurs around 355.1 °C, with a total mass loss of approximately 40% (Supplementary Fig. 10). In addition, the photothermal performance of BTP-4F (Y6) (non-quinoidal structure analogue of SKCN, Supplementary Fig. 11) under 1064 nm laser irradiation was evaluated. As shown in Supplementary Fig. 12, the temperature exhibited almost no increase with rising laser power or higher concentration. The fundamental reason lies in the fact that Y6, due to its relatively wide bandgap (HOMO/LUMO: −5.68 eV/-3.87 eV), cannot effectively absorb 1064 nm laser light (Supplementary Fig. 13). In contrast, the introduction of a quinoidal structure in SKCN significantly reduces its bandgap (Fig. 2c), making it more suitable for photon harvesting in the NIR-II region. These results further demonstrate that the introduction of quinoidal structure significantly enhances the photothermal properties.

Beyond thermal conversion, the photodynamic properties of SN_{CaC} were assessed by evaluating reactive oxygen species (ROS) generation. The intrinsic low bandgap and planar π-stacked structure of SKCN not only enhances light absorption but also promotes intersystem crossing (ISC) from the singlet to triplet state, a process facilitated by the strong electron-accepting capability of the terminal units in the ADA system. This excited triplet state efficiently transfers energy to surrounding oxygen molecules, producing both superoxide anions ($\cdot O_2^-$) and singlet oxygen ($^1O_2$). Using 1,3-diphenylisobenzofuran (DPBF) and 9,10-anthracenediyl-bis(methylene)dimalonic acid (ABDA) as probes for $\cdot O_2^-$ and $^1O_2$ respectively. Mechanistically, upon reaction with $\cdot O_2^-$, DPBF undergoes irreversible oxidation and decomposes to 1,2-dibenzoylbenzene, resulting in a rapid decrease in its absorption intensity in the UV-visible region at around 420 nm. The anthracene moiety in ABDA can be oxidized by $^1O_2$ to form a stable endoperoxide, leading to a decrease in its UV-visible absorption peak intensity around 400 nm. The extent of this reduction is proportional to the amount of $^1O_2$ generated (Fig. 3a). Thus, DPBF and ABDA serve as suitable probes for assessing ROS generation. At 100 μg/mL SKCN and 1.0 W/cm^2 irradiation, the DPBF absorbance at 420 nm decreased by nearly 50% within 10 min, and a similar trend was observed for ABDA, which decreased by 20% at 400 nm (Fig. 3g-j and Supplementary Fig. 14-17). In contrast, the photodynamic efficiency of Y6 showed almost no improvement with increasing laser power or concentration, which further indicates that the unique structure in SKCN enhances its 1064 nm laser-induced ROS

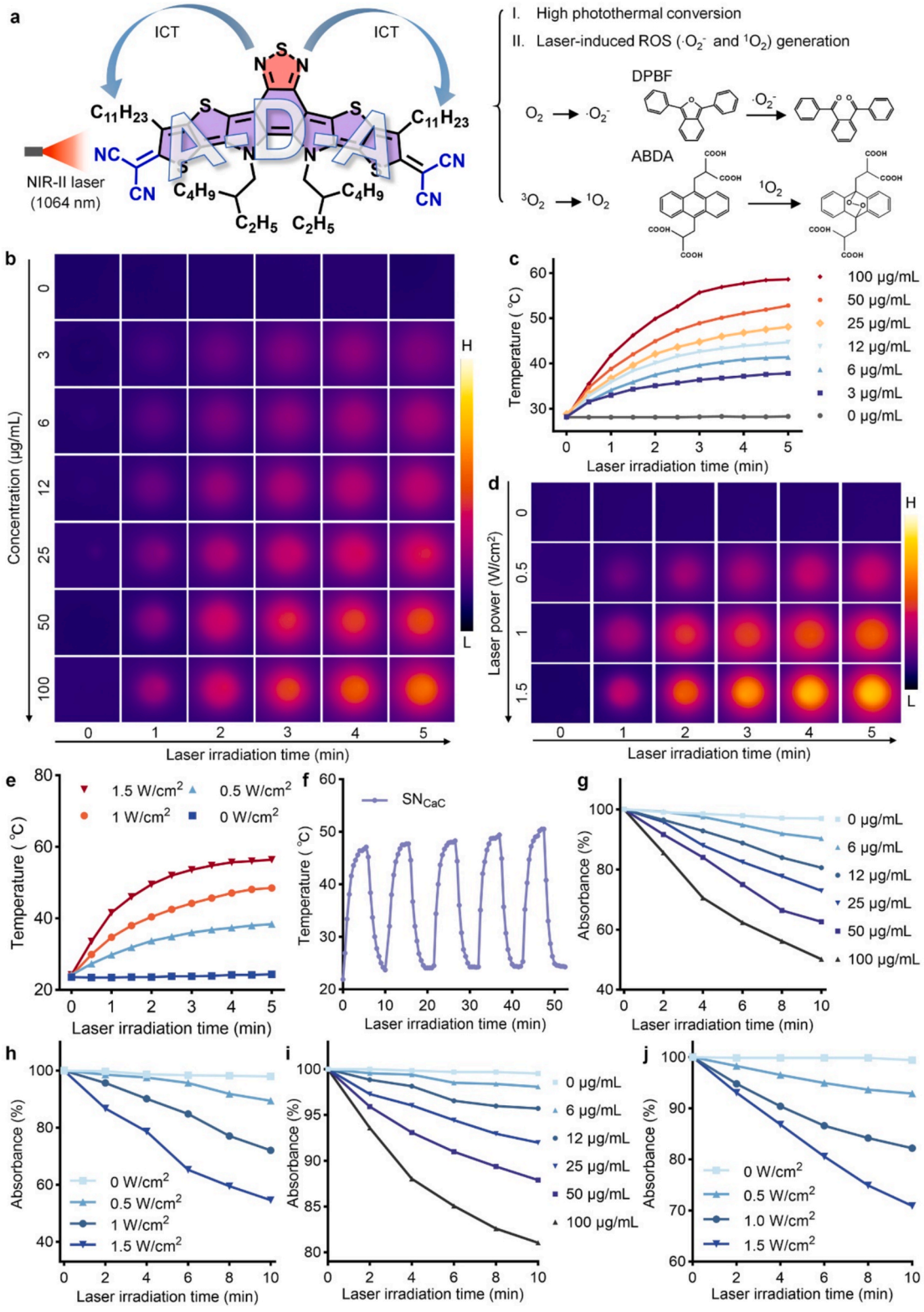

Fig. 3. Evaluation of photothermal and photodynamic performance. (a) Schematic illustration of the ADA structure, photothermal/photodynamic performance of SKCN, and the working principles of DPBF and ABDA probes. Representative thermal images (b) and temperature changes (c) of SN_{CaC} at different concentrations after 1064 nm laser irradiation (1.0 W/cm^2). Thermal images (d) and temperature changes (e) of SN_{CaC} after 1064 nm laser irradiation at different powers. (f) Five cycles of heating and cooling curves of SN_{CaC} solutions with the 1064 nm laser on–off. (g) Changes in the absorbance of DPBF in SN_{CaC} solutions with different SKCN concentrations after 1064 nm laser irradiation (1.0 W/cm^2). (h) Changes in the absorbance of DPBF in SN_{CaC} solution after 1064 nm laser irradiation at different powers. (i) Changes in the absorbance of ABDA in SN_{CaC} solutions at different concentrations after 1064 nm laser irradiation (1.0 W/cm^2). (j) Absorbance changes of ABDA in SN_{CaC} solution after 1064 nm laser irradiation at different powers.

generation efficiency (Supplementary Fig. 18-21). Importantly, the extent of ROS production was positively correlated with both the laser power and SKCN concentration, which is consistent with the photophysical behavior expected of ADA-type photosensitizers, which exhibit high intersystem crossing efficiency and strong triplet exciton generation. These findings collectively demonstrate that the SN_{CaC} system harnesses the dual photothermal and photodynamic capabilities of the ADA-structured SKCN molecule. By capitalizing on efficient NIR-II absorption, thermal conversion, and triplet-mediated ROS generation, this nanoplatform provides a powerful, light-activated therapeutic modality suitable for synergistic tumor eradication.

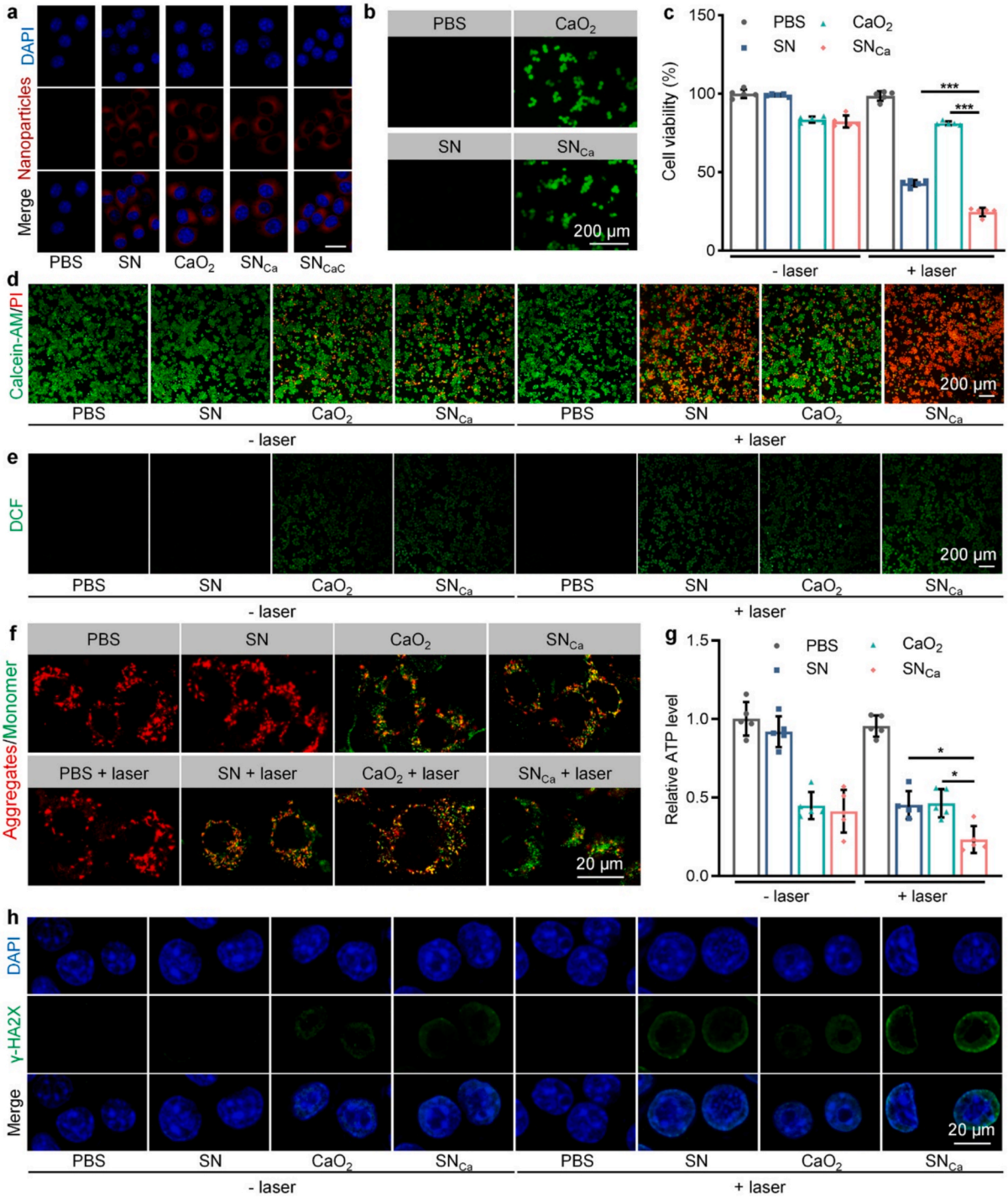

Fig. 4. Evaluation of in vitro therapeutic efficacy and mechanism. (a) Representative fluorescence images of 4T1 cells after co-incubation with PBS, SN, CaO_2, SN_{Ca} and SN_{CaC} (scale bar = 20 μm). (b) Fluorescence images of Fluo-4 in 4T1 cells after incubation with SN, CaO_2, or SN_{Ca}. (c) 4T1 cell viability after incubation with SN, CaO_2, and SN_{Ca} as well as 1064 nm laser irradiation (n = 5). (d) Fluorescence images of live/dead 4T1 cells after different treatments. Live cells were stained with calcein-AM and appear green, while dead cells were stained with PI and appear red. (e) Intracellular ROS (green fluorescence signal) detection in 4T1 cells. (f) Changes in the mitochondrial membrane potential of 4T1 cells stained with JC-1 after different treatments. (g) Intracellular ATP levels in each group (n = 5). (h) γ-H2AX levels in 4T1 cells were evaluated via immunofluorescence staining. p values were analyzed by one-way ANOVA; * indicates $p < 0.05$, and *** indicates $p < 0.001$.

In vitro therapeutic efficacy and mechanism studies

The in vitro therapeutic efficacy and mechanisms of these nanoparticles were evaluated. These nanoparticles were labeled with m-THPP for clear observation of the uptake of these nanoparticles by 4T1 cells. Significant fluorescence signals were observed in 4T1 cells after coincubation with different nanoparticles via confocal microscopy (Fig. 4a). The 4T1 cells treated with SN, CaO_2, SN_{Ca} or SN_{CaC} emitted fluorescence signals of similar intensity, which indicated the proximate uptake of these nanoparticles by the 4T1 cells (Supplementary Fig. 22). In addition, strong fluorescence signals were observed in the CaO_2- or SN_{Ca}-treated 4T1 cells loaded with the Ca^{2+} probe (Fluo-4) but not in the PBS- or SN-treated cells (Fig. 4b). The fluorescence intensity of Fluo-4 in the CaO_2- or SN_{Ca}-treated groups was 27.0-fold greater than that in the SN-treated groups because of Ca^{2+} ingestion (Supplementary Fig. 23). The influence of these nanoparticles on cell viability was evaluated via a cell counting kit-8 (CCK-8) assay. The viability of cells treated with different concentrations of SN was maintained above 92.3% (Supplementary Fig. 24). In contrast, the viability of the CaO_2- or SN_{Ca}-treated 4T1 cells decreased with increasing concentration, which could be attributed to Ca^{2+} overload. In addition, the cytotoxicity profile of SN_{CaC} is statistically indistinguishable from that of CaO_2 or SN_{Ca} across all tested concentrations (0–100 μg/mL based on SKCN). This confirms that under these conditions, the dominant cytotoxic mechanism is indeed the shared Ca^{2+} overload from the SN_{Ca} core. The combination of the 1064 nm laser resulted in a significant decrease in the viability of 4T1 tumor cells. More than 75.3% of the 4T1 cancer cells died after SN_{Ca} incubation and 1064 nm laser irradiation due to phototherapy and Ca^{2+} overload, which was significantly greater than that in the SN + laser (57.1%) and CaO_2 + laser (18.9%) groups (Fig. 4c). The results of the calcein/PI cell viability/cytotoxicity assay of 4T1 cells were similar, with significant red fluorescence (dead cells) observed in the SN + laser and SN_{Ca} + laser groups, especially in the SN_{Ca} + laser group (Fig. 4d). Similarly, Annexin V-FITC apoptosis detection revealed that 4T1 cells underwent the most severe apoptosis after SN_{Ca} incubation combined with 1064 nm laser irradiation (Supplementary Fig. 25). These results suggested that this combined treatment strategy could effectively kill 4T1 tumor cells.

The potential mechanisms of this strategy were investigated. Considering the photodynamic properties of SKCN, the ROS probe 2,7-dichlorodihydrofluorescein diacetate (DCFH-DA) was used to evaluate intracellular ROS generation after treatment. A green fluorescence signal could be observed in the SN + laser group as well as in the CaO_2 or SN_{Ca} without/with laser groups (Fig. 4e). The fluorescence intensity of the SN_{Ca} + laser group was at least 2.0-fold greater than that of the other laser-treated groups (Supplementary Fig. 26). Green fluorescence of the mitochondrial membrane potential probe (JC-1) was observed after JC-1 staining in 4T1 cells from the CaO_2, SN_{Ca}, SN + laser, and CaO_2 + laser groups, especially the SN_{Ca} + laser group, indicating a decrease in the mitochondrial membrane potential (Fig. 4f). This could be attributed to the disturbance of the mitochondrial membrane potential caused by SKCN-mediated phototherapy and Ca^{2+} overload. The intracellular ATP levels were assayed to further verify the impairment of mitochondrial function. Similarly, the SN_{Ca} + laser group presented the most obvious decrease in intracellular ATP levels (Fig. 4g). Moreover, immunofluorescence staining of γ-H2AX revealed that SN_{Ca} + laser therapy induced the most significant deoxyribonucleic acid damage (Fig. 4h). The fluorescence intensity of γ-H2AX in the SN_{Ca} + laser group was approximately 1.5- and 3.5-fold greater than that in the SN + laser and CaO_2 + laser groups, respectively (Supplementary Fig. 27). To further confirm the role of CaO_2, mitochondrial function and intracellular ATP levels were assessed using the exogenous intracellular Ca^{2+} chelator 1,2-bis (2-aminophenoxy) ethane-N,N,N,N'-tetraacetic acid (BAPTA-AM) as a Ca^{2+} scavenger. Fluorescence imaging revealed that in 4T1 cells loaded with BAPTA-AM, CaO_2 treatment induced less mitochondrial damage (green fluorescence signal) compared to CaO_2 treatment alone (Supplementary Fig. 28). Similar outcomes were observed in the SN_{Ca} + laser group and the SN_{Ca} + laser + BAPTA-AM group, indicating that the introduction of CaO_2 can enhance the disruption of mitochondrial function. Furthermore, BAPTA-AM prevented the decrease in intracellular ATP levels triggered by Ca^{2+}. Compared to CaO_2 group, BAPTA-AM loading prevented significant changes in ATP levels in 4T1 cells following CaO_2 treatment (Supplementary Fig. 29). Similarly, the ATP level in SN_{Ca} + laser + BAPTA-AM group was elevated 3.0 fold compared to that in SN_{Ca} + laser group, demonstrating the role of CaO_2 in disrupting ATP synthesis.

In vitro immunotherapy and ICD evaluation

To investigate the immunomodulatory potential of SN_{Ca} at the cellular level, we first assessed its ability to modulate PD-L1 expression in 4T1 tumor cells. While photothermal stimulation is known to induce HSP70, which stabilizes PD-L1 on the tumor cell membrane and promotes immune evasion, we hypothesized that calcium overload-mediated metabolic disruption could suppress this compensatory immune resistance mechanism. The HSP70 levels (indicated by green fluorescence signal) showed a marked increase under phototherapy alone, whereas the incorporation of calcium attenuated this light-induced upregulation (Fig. 5a). Compared to the SN + laser group, the HSP70 level in the SN_{Ca} + laser group decreased 1.4-fold (Fig. 5b). Similarly, western blot analysis further confirmed that the expression of HSP70 in the SN_{Ca} + laser group was significantly lower than that in the SN + laser group (Supplementary Fig. 30). Immunofluorescence analysis revealed that laser irradiation markedly increased PD-L1 expression in SN-treated cells, confirming the known feedback between thermal stress and PD-L1 stabilization. However, in the presence of CaO_2, particularly in the SN_{Ca} + laser group, PD-L1 expression was significantly suppressed, with the fluorescence intensity reduced to 62.2% of that observed in the SN + laser group (Fig. 5c and d). Notably, these effects were inversely correlated with Ca^{2+} clearance. Treatment with BAPTA-AM prevented the reduction in HSP70 levels observed in 4T1 cells exposed to CaO_2 or SN_{Ca} + laser. In CaO_2 + BAPTA-AM group and SN_{Ca} + laser + BAPTA-AM group, fluorescence intensity increased 6.3-fold and 1.7-fold relative to CaO_2 and SN_{Ca} + laser groups, respectively (Supplementary Fig. 31). Similar outcomes were observed in PD-L1 fluorescence imaging. The use of BAPTA-AM resulted in significantly higher PD-L1 levels following CaO_2 or SN_{Ca} + laser treatment compared to CaO_2 or SN_{Ca} + laser groups, confirming the involvement of CaO_2 in the downregulation of HSP70 and PD-L1 (Supplementary Fig. 32). These findings support the conclusion that Ca^{2+} overload-induced ATP depletion and mitochondrial dysfunction impair the biosynthetic machinery required for PD-L1 upregulation, effectively disrupting adaptive immune evasion in tumors.

Immunogenic cell death (ICD) serves as a critical bridge to activate dendritic cell (DC) maturation and initiate adaptive immune responses [33,72]. When tumor cells undergo ICD, they actively release damage-associated molecular patterns such as calreticulin (CRT) and high-mobility group box 1 (HMGB1), which act as potent “find me” and “eat me” signals. These signals are recognized by pattern recognition receptors on the surface of DCs, promoting their transition from an immature to a functionally mature state. Ultimately, this process drives the proliferation and differentiation of antigen-specific cytotoxic T lymphocytes, leading to effective antitumor immunity. Thus, we first evaluated the occurrence of ICD and its induction of DC maturation. CRT exposure and HMGB1 release, two established hallmarks of ICD, were assessed via immunofluorescence staining. Laser irradiation in the SN and SN_{Ca} groups induced moderate CRT externalization on the cell surface, with the effect being more pronounced in the SN_{Ca} + laser group because of combined photodynamic injury and calcium stress (Fig. 5e and f). In contrast, HMGB1 staining revealed a dramatic reduction in nuclear HMGB1 in the SN_{Ca} + laser group, with the fluorescence intensity decreasing by more than 28.7-fold relative to that of the untreated controls (Fig. 5g and h), indicating extensive HMGB1 release

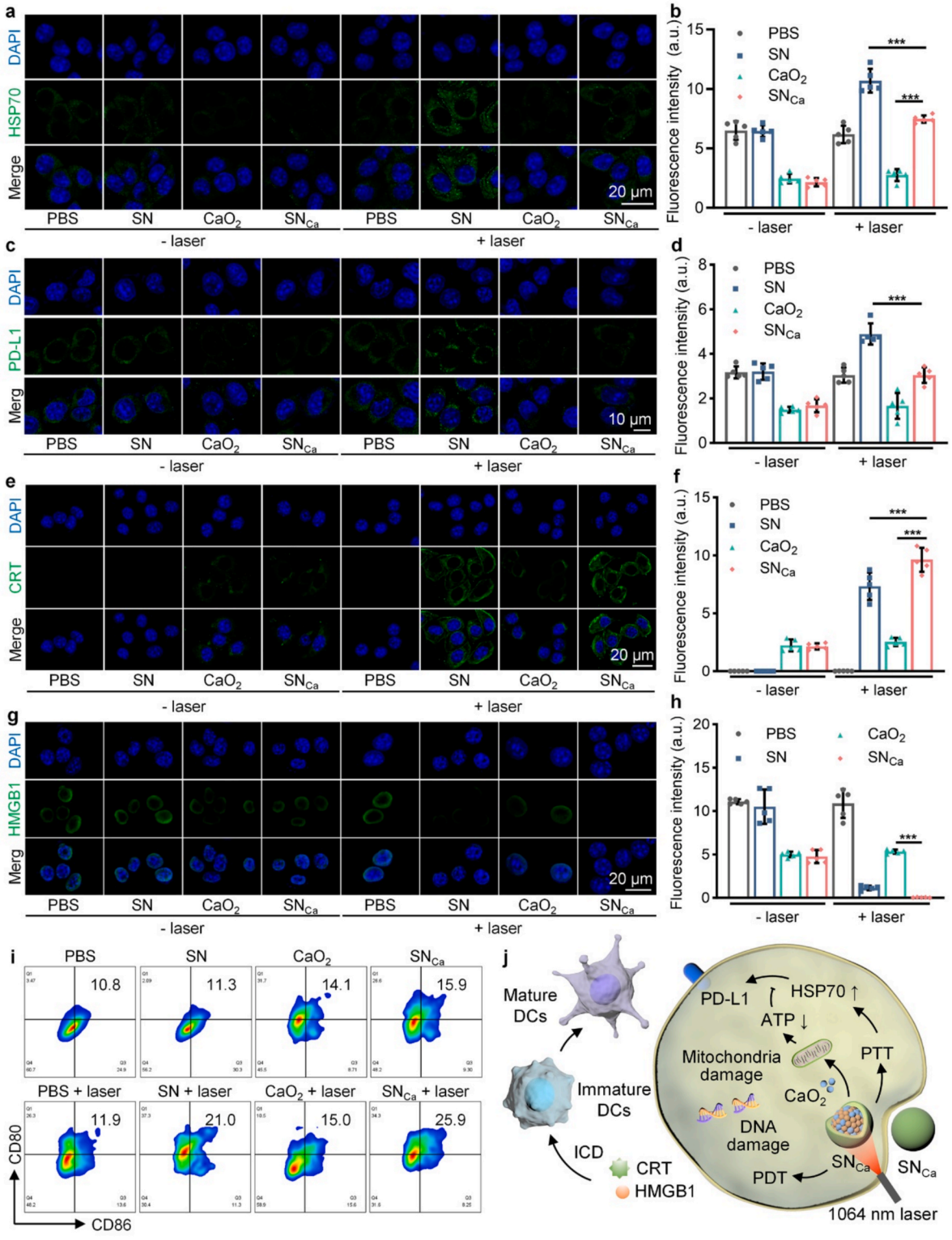

Fig. 5. In vitro effects of ICD and immunotherapy. Immunofluorescence images (a) and fluorescence intensity quantification (b) of HSP70 in 4T1 cells after different treatments (n = 5). Immunofluorescence images (c) and fluorescence intensity quantification (d) of PD-L1 in 4T1 cells after different treatments (n = 5). Immunofluorescence images (e) and fluorescence intensity quantification (f) of CRT in 4T1 cells after different treatments (n = 5). Immunofluorescence images (g) and fluorescence intensity quantification (h) of HMGB1 in 4 T1 cells after different treatments (n = 5). (i) Flow cytometry analysis of DC maturation in different treatment groups. (g) Schematic diagram of the combined immunotherapy mechanism. p values were analyzed by one-way ANOVA, *** indicates $p < 0.001$.

into the extracellular space, a signal known to promote DC recruitment and maturation. To determine whether ICD induced by SN_{Ca} could effectively activate antigen-presenting cells, we performed a transwell coculture assay in which bone marrow-derived dendritic cells (BMDCs) were used to treat 4T1 cells. Flow cytometry analysis revealed that the proportion of $CD80^+CD86^+$ mature DCs was significantly elevated in the SN_{Ca} + laser group (Fig. 5i), with a 1.2-fold increase compared with that in the other treatment groups (Supplementary Fig. 32). This enhanced

DC maturation reflects not only the presence of ICD-related damage-related molecular patterns (e.g., CRT and HMGB1) but also the alleviation of PD-L1-mediated immunosuppression, allowing DCs to more effectively initiate T cell priming. Mechanistically, this in vitro immune activation paradigm demonstrates a strategically integrated dual-axis effect: on the one hand, the SN_{Ca} + laser induces immunogenic tumor cell death via ROS, Ca^{2+} overload, and mitochondrial dysfunction; on the other hand, it counteracts PD-L1 stabilization via metabolic interference, facilitating antigen presentation and DC maturation (Fig. 5j). These synergistic effects serve as a molecular-level prelude to the systemic immune activation observed in vivo, underscoring the potential of SN_{Ca} to remodel immunologically "cold" tumors into "hot" microenvironments responsive to immunotherapy.

Tumor accumulation and in vivo therapeutic effects

Before the efficacy of this treatment strategy was evaluated, tumor accumulation and biodistribution were first examined. m-THPP was incorporated into these nanoparticles in vivo after intravenous administration. Different nanoparticles were administered intravenously to orthotopic breast cancer model mice. An in vivo imaging system revealed that the fluorescence signal at the tumor site gradually increased over time (Fig. 6a). Quantitative analysis revealed that the fluorescence intensity at the tumor site reached a maximum at 24 h after administration (Supplementary Fig. 34). The fluorescence intensity of tumors in mice treated with SN, SN_{Ca}, or SN_{CaC} was similar, indicating that these nanoparticles had similar passive accumulation effects. Due to the shielding of fluorescence signals from internal organs by hair [73,74], the major organs and tumors were further separated from the mice to observe the biodistribution of these nanoparticles. Fluorescence images of isolated tissues revealed that these nanomedicines accumulate the most in tumors (Fig. 6b). The fluorescence signal in tumors was at least 2.9-fold stronger than that in other organs (heart, liver, spleen, lung and kidney) (Supplementary Fig. 35). A thermal imager was subsequently used to record the temperature changes at the tumor site after irradiation with a 1064 nm laser. The temperature at the tumor site increased with prolonged irradiation time (Supplementary Fig. 36). After 10 min of 1064 nm laser (1.0 W/cm^2) irradiation, the temperature of the tumor sites in the mice treated with SN, SN_{Ca}, or SN_{CaC} was approximately 13.3 °C higher than that in the PBS-treated group. These results indicated that these nanoparticles could effectively accumulate in tumor tissues and achieve photothermal conversion in vivo.

The treatment plan was formulated on the basis of the enrichment effect of nanoparticles at the tumor site, and light irradiation was applied when the accumulation reached the maximum level (Fig. 6c). Orthotopic breast cancer model mice were randomly divided into PBS, SN_{Ca}, SN_{CaC}, SN + laser, SN_{Ca} + laser and SN_{CaC} + laser groups and subjected to different treatments. Continuous recording of tumor volume revealed that the tumor volume increased slowly or decreased in the SN + laser, SN_{Ca} + laser, and SN_{CaC} + laser groups (Supplementary Fig. 37). Fourteen days after the end of treatment, the relative tumor volume in the SN_{CaC} + laser group (0.3) was significantly lower than that in the PBS (13.7), SN_{Ca} (11.0), SN_{CaC} (9.8), SN + laser (3.8) and SN_{Ca} + laser (1.9) groups (Fig. 6d). SN_{CaC} + laser treatment significantly reduced the tumor burden (Fig. 6e). The weights of the tumors in the SN_{CaC} + laser group were at least 5.1-fold lower than those in the other groups (Fig. 6f). The median survival time of the mice in the PBS, SN_{Ca} and SN_{CaC} groups did not exceed 30 days. In contrast, the survival rate of the mice in the SN + laser and SN_{Ca} + laser groups remained at 60% 50 days posttreatment, and notably, no mice in the SN_{CaC} + laser group died throughout the entire process (Fig. 6g).

Moreover, the treatment effects of each group were further evaluated via hematoxylin and eosin (H&E) staining and terminal deoxynucleotidyl transferase dUTP nick-end labeling (TUNEL) staining. Remarkable chromatin condensation and nuclear fragmentation were observed in the tumor sections of the groups subjected to laser irradiation (SN + laser, SN_{Ca} + laser and SN_{CaC} + laser groups), particularly in the SN_{CaC} + laser group, which indicated severe apoptosis (Fig. 6h). Similarly, obvious fluorescence signals were observed after TUNEL staining of sections prepared from tumors in the SN + laser, SN_{Ca} + laser and SN_{CaC} + laser groups, which indicated that significant apoptosis occurred in these groups after treatment (Fig. 6i). The SN_{CaC} + laser group presented the most severely apoptotic tumor cells, with a fluorescence intensity at least 1.2-fold greater than that of the other groups (Fig. 6j). PD-L1 levels in the different treated tumors were subsequently evaluated via immunofluorescence staining. Ca^{2+} effectively alleviated the upregulation of PD-L1 induced by phototherapy (Fig. 6k). While the relative fluorescence intensity in the SN + laser group remained at 1.6, the SN_{Ca} + laser and SN_{CaC} + laser groups were able to maintain relative signal intensities comparable to those of the control group, remaining at approximately 1.1 (Fig. 6l).

Capsaicin-enhanced antitumor immunotherapy evaluation

Primary dorsal root ganglia (DRG) cells were used to investigate the regulation of neuro-immunity by capsaicin both in vitro and in vivo. Immunofluorescence staining of c-fos was used to evaluate the excitability of DRG cells stimulated with capsaicin nanoparticles. As shown in Fig. 7a, DRG cells stimulated with capsaicin nanoparticles presented increased levels of c-fos, which could be attributed to capsaicin-induced Ca^{2+} influx through the activation of TRPV1. The effects of DGR cell activation on DCs were subsequently investigated via the Transwell system (Fig. 7b). Although the increased excitability of DRG cells promoted 4T1 tumor cell proliferation, this effect was limited (Supplementary Fig. 38). In addition, capsaicin-stimulated neurons promoted the secretion of IL-12 by DCs (Fig. 7c). Furthermore, flow cytometry results showed that the proportion of $CD80^+CD86^+$ DCs was significantly increased in the group treated with activated DRG (Capsaicin nanoparticle + DRG group) (Fig. 7d). Moreover, the $CD80^+CD86^+$ DC population in the group receiving combined stimulation of activated DRG and ICD-related damage-associated molecular patterns (Supernatant + capsaicin nanoparticle + DRG group) was at least 1.4-fold higher compared to other groups (Supplementary Fig. 39). These data indicate that neural activation indeed promotes DC maturation and can synergize with ICD to further enhance DC maturation.

The adjuvantization of neural signals was subsequently evaluated in vivo and combined with phototherapy and Ca^{2+} overload (Fig. 7f). Flow cytometry analysis revealed that the $CD80^+CD86^+$ DC population was significantly increased in tumors treated with the combination of the nanobackpack and the 1064 nm laser (Fig. 7g). Compared with SN_{Ca} + laser treatment, SN_{CaC} + laser-mediated treatment increased the proportion of $CD80^+CD86^+$ DCs in the tumor site by 16.7% (Supplementary Fig. 40). In addition, T-cell infiltration at the tumor site significantly increased (Fig. 7h and i). Compared with those in the SN + laser (27.6%) and SN_{Ca} + laser (32.8%) groups, the proportion of $CD3^+CD8^+$ T cells in tumors increased to 41.6% after treatment with SN_{CaC} + laser (Supplementary Fig. 41). Similarly, the number of $CD3^+CD4^+$ T cells in the SN_{CaC} + laser group was at least 1.2-fold greater than that in the other groups (Supplementary Fig. 42). The improvement in T-cell tumor infiltration could be attributed to the combined stimulation of DCs by neurosignals and ICD, as well as PD-L1 downregulation mediated by Ca^{2+} overload. In contrast, the proportion of regulatory T (T_{reg}) cells in tumor sites decreased (Fig. 7j). The combination of SN_{CaC} and laser irradiation reduced the T_{reg} cell population to 15.9%, which was at least 1.3-fold lower than that in the other groups (Supplementary Fig. 43). These results suggested that the activation of sensory nerves could regulate DC function, promote T-cell infiltration, and improve antitumor immunotherapy efficacy (Fig. 7e).

In addition, flow cytometry was used to analyze mature DCs in the TDLN as well as $CD3^+CD4^+$ T cells and $CD3^+CD8^+$ T cells in the spleen. The population of $CD80^+CD86^+$ DCs in the TDLN significantly increased after treatment. Compared with that in the other groups, the mature DC

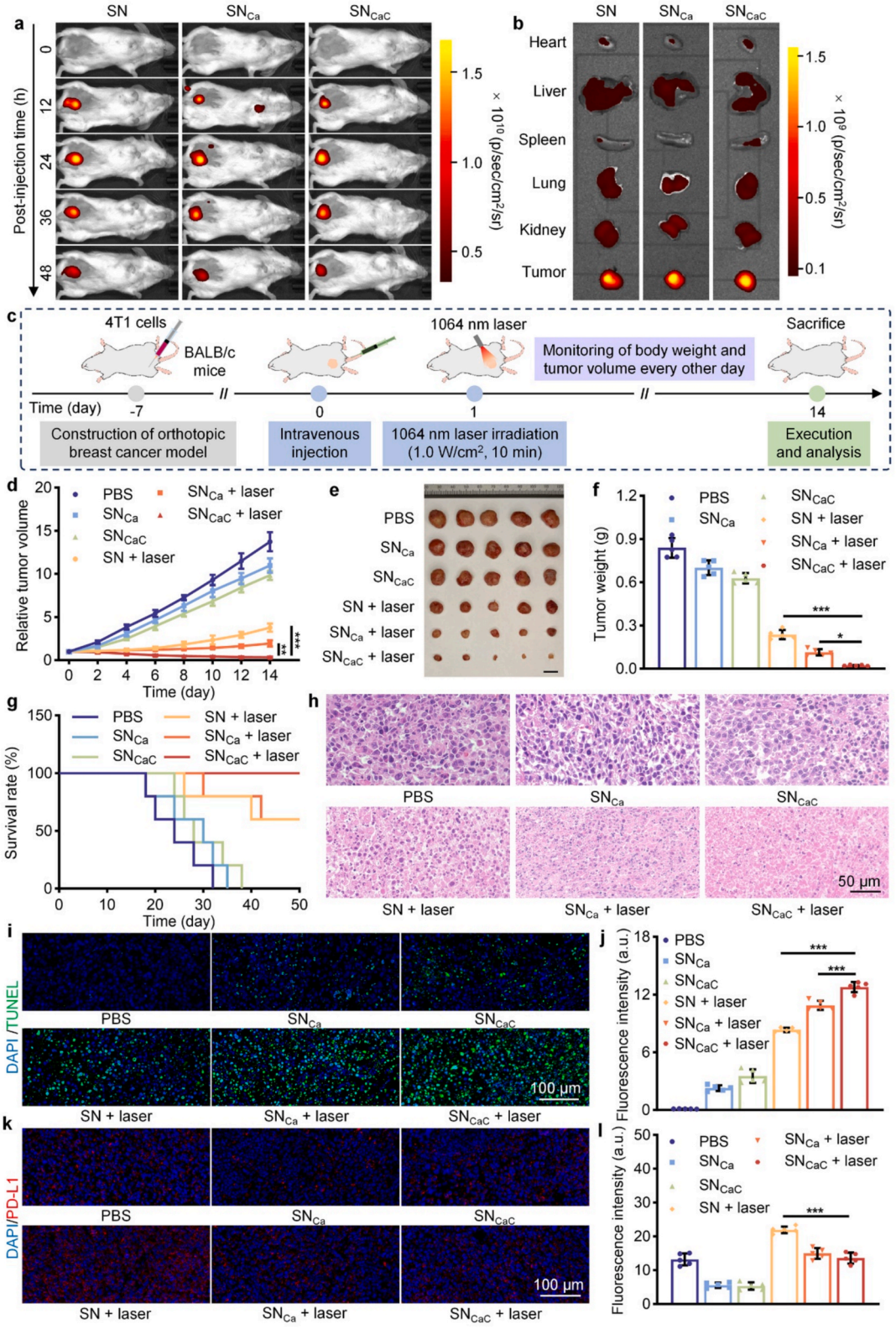

Fig. 6. In vivo accumulation and therapeutic effects. Fluorescence images of tumor accumulation (a) and biodistribution (b) in 4T1 tumor-bearing mice after intravenous administration (n = 3). (c) Illustration of the treatment process for orthotopic breast cancer model mice. Relative tumor volume (d), photograph of excised tumors (scale bar = 1 cm) (e), tumor weight (f) and survival rate (g) in each group after different treatments (n = 5). (h) Representative H&E staining images of tumors in each group after treatment. TUNEL staining images (i) and quantitative analysis (j) of tumors from mice after different treatments without/with 1064 laser irradiation (n = 5). Immunofluorescence staining images of PD-L1 (k) in each group and quantitative analysis (l) of the red fluorescence signal (n = 5). p values were analyzed by one-way ANOVA; * indicates $p < 0.05$, and *** indicates $p < 0.001$.

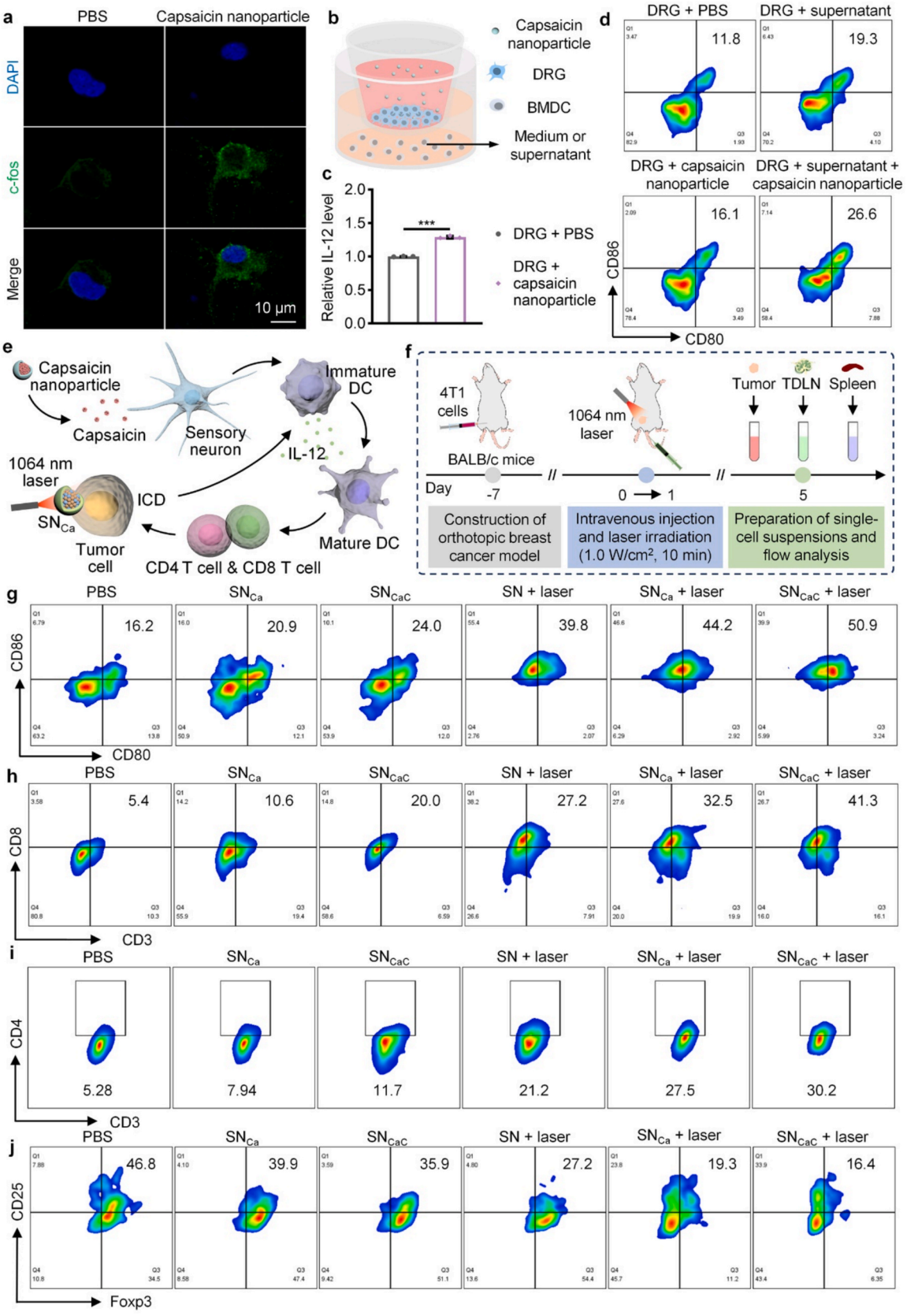

Fig. 7. Capsaicin-mediated neuroimmune regulation. (a) Immunofluorescence images of c-fos. (b) Schematic diagram of the Transwell system. (c) Relative changes in IL-12 secretion in BMDCs after different treatments (n = 3). (d) Flow cytometry analysis of mature DC populations after different types of stimulation. (e) Schematic diagram of the mechanism of combination immunotherapy. Illustration of the treatment process for orthotopic breast cancer model mice (f) and flow cytometry analysis of mature DCs (g), $CD8^+$ T cells (h), $CD4^+$ T cells (i), and T_{reg} cells (j) in the tumor sites of mice after different treatments (n = 3). p values were analyzed by two-tailed unpaired t tests; *** indicates $p < 0.001$.

population in the TDLN was approximately 1.1-fold greater in the SN_{CaC} + laser group (Supplementary Fig. 44). After treatment with SN_{CaC} combined with 1064 nm laser irradiation, the proportions of $CD3^+CD8^+$ T cells and $CD3^+CD4^+$ T cells in the spleen increased. The proportion of $CD3^+CD8^+$ T cells in the spleens of the mice in the SN_{CaC} + laser group increased by approximately 3.9% compared with that in the SN_{Ca} + laser group (Supplementary Fig. 45). Similarly, the proportion of $CD3^+CD4^+$ T cells in the spleen was significantly greater in the SN_{CaC} + laser group (28.3%) than in the SN_{Ca} + laser group (25.4%) (Supplementary Fig. 46). These results further confirmed that this treatment strategy could achieve effective immune mobilization.

RNA sequencing analysis of tumor sites after SN_{CaC} treatment

To further elucidate the mechanism of this therapeutic strategy, whole-genome RNA sequencing was used to evaluate the effects of SN_{CaC} + laser treatment on the transcriptome of tumor tissues. Principal component analysis (PCA) revealed that the SN_{CaC} + laser treatment group and the control group were clearly separated in the PC1 and PC2 dimensions, which suggested that SN_{CaC} + laser treatment significantly affected the overall gene expression profile (Fig. 8b). Compared with the PBS group, the SN_{CaC} + laser treatment upregulated 599 significantly differentially expressed genes (DEGs) and downregulated 592 DEGs (Fig. 8c).

Gene Ontology (GO) and Kyoto Encyclopedia of Genes and Genomes (KEGG) enrichment analyses were performed to identify the major affected pathways and key regulatory genes. The treatment prominently altered pathways related to cellular response to oxidative stress, ATP biosynthetic process, immune response, p53 signaling, PI3K-Akt signaling, antigen processing and presentation, and respiratory electron transport (Fig. 8d-f). Notably, the up-regulation of neural-signaling genes (Nrxn1, Syn1), DC-maturation-related genes (Flt3l, Irf7, Il27), and chemokine genes (Ccl17, Ccl22, Ccl6) provided molecular evidence for enhanced neuro-immune crosstalk, improved antigen presentation, and increased immune-cell recruitment. Conversely, down-regulation of oxidative-damage-resistance genes (Hmox1, Cox17), ATP-synthesis-related genes (Atp6v0c, Atp2a1, Atp6v1g2), immunosuppressive genes (Ido1, Tgfbr3l), and apoptosis-resistance genes (Mdm4, Trim39) indicated a suppression of tumor metabolic adaptation and immune evasion. These transcriptomic changes collectively support that the nanobackpack orchestrates a multi-modal attack on tumors by simultaneously enhancing phototherapeutic efficacy, disrupting metabolic defense, and activating systemic antitumor immunity.

Biosafety evaluation

In addition to therapeutic efficacy, the biosafety profile of SN_{CaC} was critically evaluated to assess its translational potential. Throughout the treatment period, the body weights of all the mice across the different experimental groups remained stable without an observable decline (Supplementary Fig. 47), suggesting that systemic toxicity or the stress response was negligible. This is particularly important, as fluctuations in body weight often serve as sensitive early indicators of adverse metabolic or inflammatory effects.

To further investigate potential histopathological alterations, hematoxylin and eosin (H&E) staining was performed on major organs, including the heart, liver, spleen, lungs, and kidneys, from the mice after treatment. Histological sections revealed no evidence of tissue damage, inflammation, necrosis, or architectural disruption in any of the treatment groups, including the SN_{CaC} + laser cohort (Supplementary Fig. 48).

Furthermore, after intravenous administration, the serum biochemical indicators including aminotransferase (ALT), alanine aspartate aminotransferase (AST), alkaline phosphatase (ALP), creatinine (CRE), and blood urea nitrogen (BUN) in the SN_{CaC} group showed no significant changes compared to the control group. This indicates that SN_{CaC} did not cause detectable adverse effects on liver and kidney function, providing important supporting evidence for its biosafety (Supplementary Fig. 49). The absence of pathological abnormalities confirmed that the photothermal and calcium-mediated cytotoxic effects induced by SN_{CaC} were selectively confined to tumor tissues, with minimal off-target effects. Notably, the nanoformulation components PEI, SKCN, CaO_2, and DSPE-PEG demonstrated favorable biocompatibility under the employed dosage regimens. The controlled tumor-specific activation (via pH-responsive capsaicin release and localized NIR-II irradiation) further reduced the risk of systemic immune or oxidative burden. Collectively, these results underscore the excellent biocompatibility of the SN_{CaC} system. By ensuring spatially restricted therapeutic activity and avoiding damage to normal tissues, this nanoplatform fulfills critical preclinical safety criteria and supports its candidacy for future translational and clinical development.

The long-term metabolic profile of the nanobackpack was further evaluated. The pronounced hepatic uptake observed in Supplementary Fig. 35 suggests that the nanobackpacks may be cleared via the mononuclear phagocyte system and subsequent hepatic processing. A separate long-term biodistribution and clearance study was conducted to fully characterize the metabolic fate. After administration, fluorescence signal from the liver of mice gradually decreased and disappeared completely by day 21, with no residual accumulation detected in major organs (heart, liver, spleen, lungs, kidneys) (Supplementary Fig. 50 and 51). A similar trend was observed in mouse feces (Supplementary Fig. 52). This clearance profile is consistent with similar biodegradable nanosystems reported in the literature [70,75,76]. These data indicate that SN_{CaC} was completely cleared from the body within 21 days post-administration, primarily through fecal excretion, supporting the favorable long-term biosafety profile of the nanobackpack.

Conclusions

Breast cancer stands as one of the most prevalent malignancies globally, characterized by high incidence and mortality rates, and has emerged as a leading threat to women's health worldwide. While emerging therapies such as immunotherapy and phototherapy offer promising alternatives to conventional radio-chemotherapy-based regimens, their efficacy remains constrained by several factors. These include the suboptimal phototherapeutic performance inherent to traditional organic photosensitizers due to their wide bandgap, the immunosuppressive tumor microenvironment, and therapy resistance under stress conditions. In this study, a demountable quinoidal semiconductor nanobackpack was designed for combinatorial NIR-II photoimmunotherapy of breast cancer, which could enhance the phototherapeutic efficacy of organic components, counteract HSP-mediated therapeutic resistance, and mobilize neuro-immune activity. The nanosystem exhibited superior photothermal and photodynamic properties, suppresses HSPs-driven thermotolerance and immune evasion, and further promotes antitumor immune mobilization via sensory neuron activation, thereby inhibiting tumor growth in breast cancer mouse model.

The introduction of the quinoidal structure plays a pivotal role in enhancing the phototherapeutic performance of organic materials. The incorporation of the quinoidal structure lead to greater delocalization of the π-electron, resulting in more uniform bond lengths and a reduced bandgap in SKCN. DFT calculations estimated the bandgap of SKCN to be 1.1 eV, which enhanced its light absorption efficiency and increased the probability of non-radiative transitions. Furthermore, as a fully fused π-conjugated molecule, SKCN exhibited high structural rigidity, which suppressed vibrational coupling between the S_1 and S_0 states. This favors excitation energy transfer to the triplet state via ISC, thereby improving the photodynamic performance. The strategy of introducing quinoidal structure is particularly valuable for enhancing the NIR-II phototherapeutic efficacy of organic materials.

Beyond enhancing intrinsic light absorption and conversion

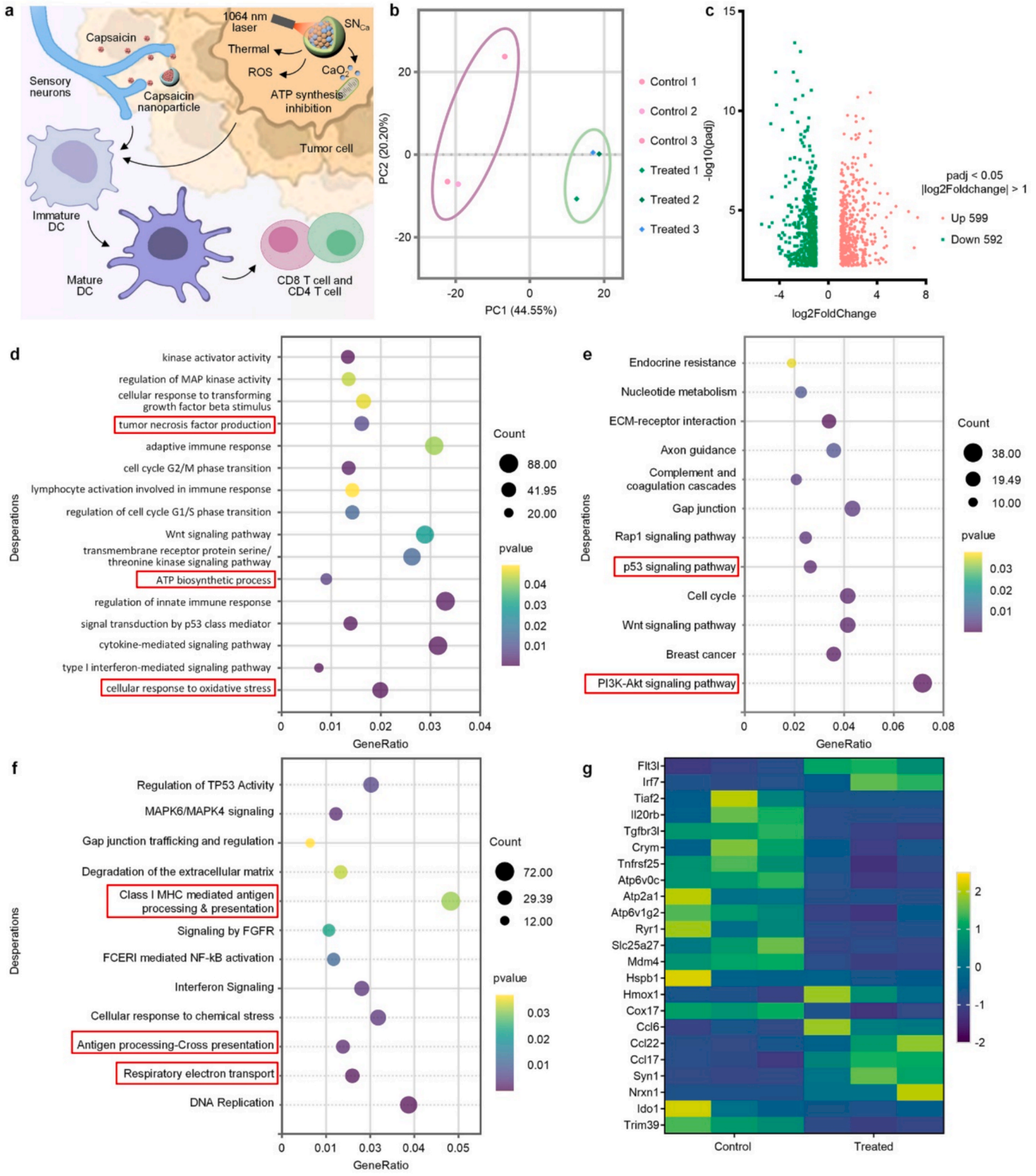

Fig. 8. RNA transcriptomics analysis of tumor tissue after treatment. (a) Scheme of therapeutic mechanism of SN_{CaC} in breast cancer. (b) PLS-DA of the PBS and SN_{CaC} + laser groups. (c) Volcano plot of the downregulated or upregulated DEGs in the SN_{CaC} + laser group compared with those in the PBS group. (d) GO analysis of the PBS and SN_{CaC} + laser groups. (e) KEGG enrichment analysis showing the pathways in which differentially expressed genes in the SN_{CaC} + laser group versus the PBS group were enriched. (f) Reactome functional enrichment analysis of the PBS and SN_{CaC} + laser groups. (g) Heatmap of differential gene expression between the PBS and SN_{CaC} + laser groups (n = 3).

efficiency, this nanobackpack could mitigate thermal resistance and immune evasion by attenuating the therapy-induced stress response. Tumor cells could upregulate HSP expression during photothermal therapy, which could not only enhance thermal tolerance leading to diminished therapeutic efficacy but also stabilize PD-L1 on the tumor surface, thereby impairing immunotherapy outcomes. The incorporation of CaO_2 into the nanobackpack effectively disrupted mitochondrial homeostasis, leading to ATP depletion and subsequent inhibition of HSP function. Experimental results confirmed that CaO_2 doping could impair mitochondrial function, reduce intracellular ATP levels, and thereby potentiate phototherapeutic efficacy while suppressing PD-L1 upregulation.

To further enhance the activation of antitumor immune responses, the capsaicin nanoparticles are designed to be released in the tumor microenvironment to promote DC maturation by modulating sensory neuron activity for the augmentation of tumor antigen presentation. Mechanistically, capsaicin activated sensory neurons via TRPV1 channel opening, which in turn facilitated DC maturation. In combination with ICD this process could significantly increase the proportion of mature DC and subsequently enhance T cell-mediated tumor killing through improved antigen presentation. This therapeutic approach upregulated c-fos level in sensory neurons, promoted DC maturation both in vitro and in vivo, and enhanced T cell infiltration. In summary, the synergy between neuro–immune modulation, ICD and disruption of PD–L1 stabilization potently enhanced antitumor immunity.

The improvements in photosensitizer performance, disruption of tumor resistance mechanisms and enhancement of antigen presentation collectively establish an effective strategy for photoimmunotherapy in breast cancer. Monitoring of tumor burden post-treatment and histological analysis revealed that this combined therapeutic strategy induced the most marked tumor ablation, apoptosis and necrosis compared to the control and counterpart-mediated treatments, significantly pronouncing extension of survival in mouse models. Furthermore, flow cytometry analysis demonstrated a substantial increase in the proportions of $CD80^+CD86^+$ DCs, $CD3^+CD4^+$ T cells and $CD3^+CD8^+$ T cells within tumor tissues, confirming the enhancement of antitumor immune responses. These findings underscore the unique advantages of the nanobackpack system in augmenting phototherapeutic outcomes, disrupting tumor defense mechanisms, and activating potent antitumor immunity.

This nanobackpack system offers several key advantages for phototherapeutic applications. The quinoidal semiconductor molecule exhibited enhanced NIR-II photothermal and photodynamic performance, effectively addressing the limitations of the constrained tissue penetration depth as well as insufficient light absorption and low energy conversion efficiency of conventional inorganic and organic materials, which might diminish therapeutic outcomes. Moreover, the nanobackpack system simultaneously mitigated tumor stress responses while executing therapeutic functions. This action could attenuate tumor thermal resistance and destabilize surface PD-L1, thereby significantly enhancing the treatment efficacy. Furthermore, the engagement of neuro-immune promoted DCs maturation, which synergized with ICD and PD-L1 downregulation to amplify antitumor immunity. Collectively, these distinctive features enable the nanobackpack to serve as a highly promising phototherapeutic agent, offering an innovative strategy for NIR-II photoimmunotherapy in breast cancer.

Looking ahead, several key challenges remain to be addressed as this strategy advances toward clinical translation. First, comprehensive safety and pharmacokinetic evaluations are warranted, including long-term biocompatibility, detailed metabolic pathways, and potential off-target neuronal activation in humanized models. In addition, laser irradiation parameters must be carefully optimized to effectively and safely penetrate human patient tissue and seamlessly integrate into existing clinical laser protocols. Furthermore, while this study demonstrates promising efficacy in breast cancer, future investigations could explore extending this neuro-immune-photo platform to other innervated solid tumors (e.g., pancreatic or prostate cancer), potentially broadening its clinical impact. Finally, scaling up the synthesis of the multi-component nanobackpack with good manufacturing practice compliance will be essential to ensure batch-to-batch consistency and clinical-grade quality.

This study presents a demountable quinoidal semiconductor nanobackpack that enhances photoimmunotherapy for breast cancer by improving the photothermal and photodynamic properties of organic photosensitizers, suppressing HSP involved in thermal resistance and immune evasion, and promoting DC maturation. This integrated platform simultaneously addresses multiple intrinsic and extrinsic challenges in breast cancer photoimmunotherapy. The proposed strategy not only establishes a new paradigm for breast cancer photoimmunotherapy but also provides fresh impetus for the optimization of organic semiconductor materials in oncological treatment.

CRediT authorship contribution statement

Yijing Zhang: Methodology. **Guangkun Song:** Methodology. **Gaoli Niu:** Investigation. **Ruiyan Li:** Methodology. **Xue Yuan:** Methodology. **Nana Ran:** Software. **Yulu Hu:** Methodology. **Tianze Du:** Investigation. **Yongsheng Chen:** Supervision, Resources. **Yong Kang:** Writing – original draft, Supervision. **Li Wang:** Writing – original draft, Supervision. **Xiaoyuan Ji:** Writing – review & editing, Supervision, Funding acquisition, Conceptualization.

Declaration of competing interest

The authors declare that they have no known competing financial interests or personal relationships that could have appeared to influence the work reported in this paper.

Acknowledgments

This study was financially supported by grants from the Beijing-Tianjin-Hebei Natural Science Foundation Cooperation Project (Grant No. 25JJJC0017, X.J.), Tianjin Science and Technology Project (Grant No. 25JCLMJC00090, X.J.), the Key Project of the Henan Provincial and Ministerial Coconstruction Program for Medical Science and Technology Research (Grant No. SBGJ202502115, G.N.), National Natural Science Foundation of China (Grant No. 32471388 and 32071322, X.J.), and National Natural Science Funds for Excellent Young Scholars (Grant No. 32122044, X.J.).

Appendix A. Supplementary data

Supplementary data to this article can be found online at https://doi.org/10.1016/j.mattod.2026.103203.

Data availability

Data will be made available on request.

References

[1] G. Bianchini, et al., Nat. Rev. Clin. Oncol. 19 (2022) 91.
[2] M.A. Harris, et al., Nat. Rev. Cancer 24 (2024) 554.
[3] *Lancet* 403(2024), 1989.
[4] J. Kim, et al., Nat. Med. 31 (2025) 1154.
[5] W.D. Foulkes, et al., N. Engl. J. Med. 363 (2010) 1938.
[6] Y. Liu, et al., Br. Med. J. 391 (2025) e085457.
[7] C.M. Perou, et al., Nature 406 (2000) 747.
[8] A.N. Giaquinto, et al., CA-Cancer J. Clin. 74 (2024) 477.
[9] G.T. Budd, et al., J. Clin. Oncol. 33 (2015) 58.
[10] J. Lee, J. Clin. Med. 12 (2023) 1524.
[11] J.A. Sparano, et al., N. Engl. J. Med. 358 (2008) 1663.
[12] Y.Y. Cai, et al., Signal Transduction Targeted Ther. 10 (2025) 115.
[13] Z.J. Xie, et al., Chem. Soc. Rev. 49 (2020) 8065.
[14] Y.J. Gao, et al., Nano-Micro Lett. 16 (2024) 21.

[15] M. Overchuk, et al., ACS Nano 17 (2023) 7979.
[16] E.J. Hong, et al., Acta Pharm. Sin. B 6 (2016) 297.
[17] T. Zhang, et al., Chem. Soc. Rev. 54 (2025) 8406.
[18] Zhu, L. Y., et al., Angew. Chem., Int. Ed. 60(2021), 15348.
[19] J.W. Song, et al., Nat. Commun. 15 (2024) 10395.
[20] G.K. Song, et al., Chem. Commun. 59 (2023) 10307.
[21] Y.Z. Zhang, et al., Adv. Mater. 35 (2023) 2211714.
[22] G.Y. Zhang, et al., Chem. Rev. 118 (2018) 3447.
[23] H.S. Jung, et al., Chem. Soc. Rev. 47 (2018) 2280.
[24] Sun, Y. L., et al., Mater. Sci. Eng., R 136(2019), 13.
[25] M.Q. Yang, et al., Chem 10 (2024) 1425.
[26] X. Zhou, et al., ACS Cent. Sci. 9 (2023) 1679.
[27] C. Hu, et al., MedComm 3 (2022) e161.
[28] X.H. Zhang, et al., Chem. Commun. 59 (2023) 3898.
[29] Z.H. Wang, et al., Adv. Sci. 4 (2017) 1600327.
[30] W.W. Ying, et al., ACS Nano 14 (2020) 9662.
[31] H.Y. Li, et al., Adv. Sci. 11 (2024) 2308251.
[32] S.Y. Liang, et al., Adv. Funct. Mater. 35 (2025) 2424108.
[33] H.T. Yuan, et al., Adv. Mater. 37 (2025) 2406662.
[34] W.Q. Zhang, et al., Nat. Commun. 15 (2024) 5670.
[35] Y. Zhao, et al., Nat. Biomed. Eng. 9 (2025) 234.
[36] S. Goswami, et al., Nat. Immunol. 25 (2024) 2186.
[37] J. Park, et al., Immunity 56 (2023) 32.
[38] T. Dobie, Neuron 110 (2022) 3407.
[39] N. Khanmammadova, et al., Trends Cancer 9 (2023) 636.
[40] R. Mancusi, M. Monje, Nature 618 (2023) 467.
[41] F. Winkler, et al., Cell 186 (2023) 1689.
[42] M. Monje, F. Winkler, Nat. Neurosci. 28 (2025) 915.
[43] D.D. Shi, et al., Lancet Oncol. 23 (2022) e62.
[44] T. Crosson, et al., Immunity 58 (2025) 1161.
[45] L.W. Deng, et al., Immunity 57 (2024) 815.
[46] C.R. Donnelly, et al., Trends Neurosci. 43 (2020) 822.
[47] Erin, N., et al., Brain, Behav., Immun. 48(2015), 174.
[48] S.Y. Huang, et al., Cell 184 (2021) 441.
[49] S. Udit, et al., Nat. Rev. Neurosci. 23 (2022) 157.
[50] M.J. Caterina, et al., Nature 389 (1997) 816.
[51] D.H. Kwon, et al., Nat. Struct. Mol. Biol. 28 (2021) 554.
[52] F. Yang, et al., Nat. Chem. Biol. 11 (2015) 518.
[53] R. Dantzer, Physiol. Rev. 98 (2018) 477.
[54] Erin, N., Cancer Immunol., Immunother. 69(2020), 307.
[55] B.M. Janelsins, et al., Blood 121 (2013) 2923.
[56] C.S. Garris, et al., Immunity 49 (2018) 1749.
[57] Y.Z. Li, et al., Nat. Cancer 1 (2020) 882.
[58] G. Trinchieri, Nat. Rev. Immunol. 3 (2003) 133.
[59] C. Bao, et al., Adv. Funct. Mater. 31 (2021) 2011130.
[60] A.M. Bode, Z.G. Dong, Cancer Res. 71 (2011) 2809.
[61] X.Y. Ma, et al., Adv. Funct. Mater. (2025) 2423036.
[62] T.L.H. Ngo, et al., ACS Nano 18 (2024) 5632.
[63] Sampedro, A., et al., Angew. Chem., Int. Ed. 57(2018), 17235.
[64] Y.D. Guo, et al., J. Am. Chem. Soc. 146 (2024) 10217.
[65] Hu, J. J., et al., Angew. Chem., Int. Ed. 63(2024), e202317578.
[66] Zhang, Z. R., et al., Sci. Adv. 10(2024), eadl0263.
[67] Z.Z. Li, et al., Adv. Sci. 12 (2025) e2403077.
[68] G.Y. Sha, et al., Int. Immunopharmacol. 122 (2023) 110492.
[69] R.M. Vabulas, et al., J. Biol. Chem. 277 (2002) 15107.
[70] G. Niu, et al., Adv. Mater. 37 (2025) 2415189.
[71] X. Yuan, et al., Nat. Commun. 14 (2023) 5140.
[72] Yang, Z., et al., Sci. Adv. 11(2025), eadw0797.
[73] Y. Hoshino, et al., Exp. Anim. 66 (2017) 437.
[74] H.Y. Yang, et al., J. Am. Chem. Soc. 147 (2025) 30794.
[75] Li, J. C., et al., Angew. Chem., Int. Edit. 62(2023), e202305200.
[76] Y.J. Zhang, et al., Adv. Funct. Mater. 35 (2025) 2412165.